

A UNIFIED APPROACH TO STATISTICAL
CLASSIFICATION OF BURIED OBJECTS FROM
SPATIALLY SAMPLED ELECTROMAGNETIC
INDUCTION DATA

A Thesis Presented

by

Beeta Tarokh

to

Electrical and Computer Engineering

in partial fulfillment of the requirements

for the degree of

Masters of Science

in

Electrical and Computer Engineering

Northeastern University

Boston, Massachusetts

May 2003

© Copyright by Beeta Tarokh 2003
All Rights Reserved

NORTHEASTERN UNIVERSITY
Graduate School of Engineering

Thesis Title: A Unified Approach to Statistical Classification of Buried Objects from Spatially Sampled Electromagnetic Induction Data.

Author: Beeta Tarokh.

Department: Electrical and Computer Engineering.

Approved for Thesis Requirements of the Masters of Science Degree:

Thesis Advisor: Prof. Eric Miller	Date
Thesis committee: Prof. Dana Brooks	Date
Thesis Committee: Prof. Carey Rappaport	Date
Department Chair: Prof. Fabrizio Lombardi	Date
Director of the Graduate School: Prof. Yaman Yener	Date

NORTHEASTERN UNIVERSITY
Graduate School of Engineering

Thesis Title: A Unified Approach to Statistical Classification of Buried Objects from Spatially Sampled Electromagnetic Induction Data.

Author: Beeta Tarokh.

Department: Electrical and Computer Engineering.

Approved for Thesis Requirements of the Masters of Science Degree:

Thesis Advisor: Prof. Eric Miller

Date

Thesis committee: Prof. Dana Brooks

Date

Thesis Committee: Prof. Carey Rappaport

Date

Department Chair: Prof. Fabrizio Lombardi

Date

Director of the Graduate School: Prof. Yaman Yener

Date

Copy Deposited in Library:

Reference Librarian

Date

Acknowledgements

During the time I worked on this project, many people have knowingly or not provided me with invaluable help and guidance. First and foremost, I wish to thank my advisor Professor Eric Miller, for the opportunity, support, inspiration and guidance necessary for this research.

I would also like to thank my committee members Professor Rappaport and Professor Brooks for reading my thesis and providing me with constructive comments and criticism.

I also wish to thank my mom and my brothers Vahid and Saeed for their love and support and for continuously asking me when I was going to graduate. I would like to thank friends and loved ones for their support as well. A special thank you goes to Andrew Brzezinski for making the past couple of years the most magical years of my life.

I would also like to thank my colleagues at Northeastern, especially those at NWIIRL for numerous valuable discussions.

Finally, I would like to thank SERDP, taxpayers and the government of the United States for providing the financial support that made this project possible.

Contents

Acknowledgements	v
List of Figures	vi
List of Tables	vii
1 Introduction	8
1.1 Background	8
1.2 Literature Survey	8
1.3 Organization	8
2 Problem formulation and Physical Model	9
2.1 Electromagnetic Induction Sensors	9
2.1.1 Bistatic Sensors	9
2.1.2 Monostatic Sensors	10
2.1.3 GEM-3 Sensor	10
2.2 Physical Model	11
2.2.1 Euler Angles	17
3 Processing Method	24
3.1 Library Construction	24
3.2 Parameter Estimation	26
3.2.1 Estimation When Sensor Locations are Known	26
3.2.2 Estimation When Sensor Locations are Unknown	26
3.2.3 Boxes	31
3.2.4 Ellipsoids	31
3.3 Classification	34
4 Numerical Examples	36

4.1	Processing When Sensor Locations Are Known	36
4.1.1	Simulated Data	36
4.1.2	The Geophex Pipe Data	44
4.1.3	The JPG-IV Data	48
4.2	Processing When Sensor Locations Are Unknown	51
4.2.1	Ellipsoids	51
4.2.2	Boxes	52
5	Conclusion and Future Work	53
A	Pole Values for Monte Carlo Analysis	55
	Bibliography	58

List of Figures

2.1	Geometry of sensor coils and target object for one sensor.	12
2.2	Euler Angles.	18
2.3	Rotation of the coordinate system about the Z axis through an angle ϕ .	19
2.4	Rotation of the coordinate system about the X' axis through an angle θ .	19
2.5	Rotation of the coordinate system about the Z_2 axis through an angle ψ .	20
4.1	Effective Pole Distribution for Amorphous Targets With Pole Switching.	39
4.2	Effective Pole Distribution for Amorphous Targets Without Pole Switching.	40
4.3	Effective Pole Distribution for Pipe-like Targets With Pole Switching.	40
4.4	Effective Pole Distribution for Pipe-like Targets Without Pole Switching.	41
4.5	Effective Pole Distribution for Sphere-like Targets With Pole Switching.	41
4.6	Effective Pole Distribution for Sphere-like Targets Without Pole Switching.	42
4.7	Pole Locations for Geophex Data Library.	46
4.8	Geophex UXO Site, Raleigh, NC.	47
4.9	Pole Locations for JPG-IV Data Library.	50

List of Tables

4.1	Orientations Used to Construct the Simulated Data.	37
4.2	Simulated Data Pole Library for Amorphous Targets.	38
4.3	Simulated Data Pole Library for Pipe-Like Targets.	38
4.4	Simulated Data Pole Library for Sphere-Like Targets.	38
4.5	Classification Results for Monte Carlo Analysis without Pole Switching.	42
4.6	Classification Results for Monte Carlo Analysis with Pole Switching.	43
4.7	Bounds for Monte Carlo Analysis.	43
4.8	Classification Results for Monte Carlo Analysis.	45
4.9	GEM 3 Pipe Data Pole Library.	46
4.10	GEM 3 Pipe Data Results.	48
4.11	JPG-IV GEM 3 Targets.	49
4.12	JPG-IV GEM 3 Data Pole Library.	49
4.13	JPG-IV Data Results.	51
4.14	Classification Results for Unknown Sensor Locations (Ellipsoids).	52
4.15	Classification Results for Unknown Sensor Locations (Boxes).	52
A.1	Pole Values for Monte Carlo Analysis for Amorphous Targets.	56
A.2	Pole Values for Monte Carlo Analysis for Pipe Like Targets.	56
A.3	Pole Values for Monte Carlo Analysis for Sphere Like Targets.	57

Abstract

The main goal of this work is to introduce and develop methods for classification of objects based on spatially sampled electromagnetic induction data taken in the time or frequency domain. To deal with nuisance parameters associated with the position of the object relative to the sensor as well as the orientation of the object, a computationally tractable physical model explicit in these unknowns is developed.

The physical model presented in this work is parameterized by a collection of Laplace-plane poles whose values in theory are independent of object position and orientation and hence can be used as features for classification. The overall algorithm for our pole-based approach consists of two stages. First we estimate the values of the unknown parameters and then we perform classification. Classification is done by comparing either the raw data or some low-dimensional collection of features extracted from the data to entries in a library. The library is constructed using either simulated or calibration data. Given the library, the processing scheme consists of two stages. First, a maximum likelihood method is developed and analyzed for the problem of joint pole, location, and orientation parameter determination. Second, the extracted pole values are fed into the classifier. We will validate our methods on both simulated and field data taken from frequency domain sensors. Preliminary results on synthetic data indicate the robustness of the pole estimates as features for classification and point toward the need for further analytical as well as experimental evaluation of the proposed methods.

The second part of this work is dedicated to the investigation of practical issues in dealing with our proposed method. The problem of pole switching is one of “the issues” addressed here. As we will explain in great detail, a matrix used in our physical model to encode orientations leads to the switching of the order of the pole values used for classification. We will address the problems associated with this topic and propose a simple solution. Uncertainty in sensor position is another practical issue that we face when using real field data. In the parametric model employed in the first part of this work we assume that the locations of the transmitters and receivers

are known. However, in typical situations these positions are known to within some bounded precision in the x , y , and z directions. The effects of this additional information in the parameter extraction procedure are demonstrated through the use of a min-max optimization procedure. Specifically, we look for the object parameters (poles, location, and rotation angles) that minimize the maximum data residual where the maximum error is computed over ellipsoids or boxes of possible sensor locations defined by the bound information. An algorithm for solving this new problem is presented and validated using simulated data.

Chapter 1

Introduction

1.1 Background

It is well known that time varying fields induce a current flow, known as eddy current, in electrically conductive and/or magnetically permeable objects placed in their vicinity [9]. We can attempt to detect and classify the aforementioned objects through the observation of the secondary magnetic field caused by the induced current. This is the basic foundation of the electromagnetic induction (**EMI**) method.

EMI method is a prominent technique used widely in detection and discrimination of conducting and ferrous targets. The subsurface sensing problem is a specific example, where the EMI method is used to sense buried metal mines and unexploded ordnance (**UXO**). A typical assumption (and one that was used in this work) is that the target resides in free space because the conductivity of such targets is typically many orders of magnitude larger than the conductivity of soil [7].

EMI systems usually operate at very low frequencies, specifically less than $1MHz$. At these frequencies the displacement current component in the near-field loop-induced fields can often be ignored. This means that, such systems are in reality insensitive to dielectric discontinuities and primarily sensing changes in conductivity and permeability. As expected, EMI systems are of primary use in sensing applications where the target is substantially metallic [6].

Our main interest in this work is the frequency dependence of the EMI response.

By using an object's EMI response in the frequency domain, we try to characterize the object's geometry and material composition. The EMI response of a conducting and ferrous target is determined by EMI resonant frequencies, which exist along the imaginary axis of the complex-frequency plane [9]. Here we only use the ω plane for complex frequencies. Assuming an $\exp(j\omega t)$ time dependence, a purely imaginary resonant frequency corresponds to the exponential decay characteristic of time-domain EMI interaction with conducting and ferrous targets. As we will explain in Section 2.2, the imaginary resonant frequencies corresponding to magnetic dipoles play an important role in characterizing the frequency and time domain properties of the magnetization tensor [5].

Extracting information such as size, shape, orientation, and type of target requires the development of advanced signal processing methods, which are tied directly to physical models of the sensor. Here, we consider a number of options for the estimation of these parameters as well as the classification of buried objects given EMI data obtained at multiple points in space in the vicinity of an already-detected object with particular attention paid to UXO and demining applications.

Classification is generally performed by comparing the raw data or some low-dimensional collection of features extracted from the data to entries of a library. The library is built from signature vectors or feature vectors from all targets of interest in a given application. The classifier selects the element of the library that gives the best fit to the data or the features. If a sufficiently good fit cannot be obtained, the classifier declares that the object under consideration is in fact not in the library. This last step is very important for the UXO and demining problems where there is a strong desire to correctly reject the clutter items, as the unnecessary removal of such items consumes both time and resources.

Most of the recent work in the area of EMI classification has been based on a simplified physical model for the interaction of the fields with the unknown target. As we describe in detail in Section 2.2, assuming that the target scatters the incident energy like a dipole [7], information concerning the class and orientation of the object in space is encoded in the magnetic polarizability tensor which is independent of the location of the object relative to the sensors. The location information is contained

in two 3×1 field vectors (see Section 2.2 for more details). Mathematically, the magnetic polarizability tensor is a 3×3 matrix which has a functional dependence on frequency. In theory, this matrix can be diagonalized by a frequency independent rotation matrix indicating the orientation of the object in space (Section 2.2.1). Each element of the resulting 3×3 diagonal matrix, which carries all of the frequency dependence, provides the scattering characteristics of the object along each of its three principal axes and are used for classification purposes. We refer to these as the principal axis polarizability functions (PAPFs).

In this work we construct a number of estimation methods based on a physical model that is the fusion of the dipole scattering model in [7] and a parametric PAPF mode explained in [14]. This model is analytical in the parameters of the PAPF, the (x, y, z) location of the object, and the three Euler angles [11] describing the rotation matrix. The relatively simple closed form nature of the model with respect to these parameters leads us to classification methods in which the orientation and location of the object are explicitly estimated along with the parameters needed for classification. Thus, our approach provides information regarding these geometric characteristics of the object. Also, the closed form nature of the PAPF model allows our approach to be applied with equal ease to both time and frequency domain sensor data.

In theory, the PAPF are comprised of an infinite number of single pole transfer functions in frequency, but in reality, since real objects do not scatter exactly as dipoles, it makes sense to consider reduced order models for the purposes of processing. Indeed, experimentally it has been shown that one or two poles can typically be used to match the model to measured data [6, 5, 16]. In this work, we propose a model in which each PAPF is represented as a one-pole transfer function. Since there are three principal axes, we estimate three pole constants as part of the classification routine (one pole per axis). Our method explicitly accounts for modeling error introduced by the fact that we are not using an exact scattering model. More specifically, because a three-pole model cannot exactly represent the data, the pole values will not be independent of object position and orientation. Rather for a given type of target, there will be a spread of pole values as a function of these geometric nuisance parameters. Thus, we introduce a simple quadratic-form classifier, which compensates

for this effect of model mismatch. Our classification scheme explicitly contains a null hypothesis that the object is in fact clutter. Thus, we provide a quantitative means of rejecting such items in the context of a multi-object classification procedure.

A new solution approach for the subsurface sensing problem given data from a sensor, which has been scanned over a region of the earth, is also proposed. In most methods it is common to assume that the positions of the sensor are known precisely at least relative to some fixed reference point, a condition which is often not met in practice. For handheld systems especially, the sensor may not be equipped with GPS in which case some sort of dead reckoning may be employed to get approximate locations. In the case of vehicular or cart mounted sensors, even with GPS, the effects of positional uncertainties have not been extensively studied for problems where one requires high resolution localization of buried objects.

The method we propose is motivated by the observation that real data sets for which positions of the sensor are recorded are often accompanied by the caveat that these locations are accurate only to within some tolerances in the x , y , and z coordinates. We approach this problem using the worst-case (or min-max) method. That is, we look for those parameters of the medium (voxel values, object characteristics, etc.) which minimize the maximum mis-fit to the data where the maximum is taken over all possible sensor locations each of which is restricted to lie within some bounded region of space. The geometric structure of these uncertainty regions is derived again from the prescribed tolerances. In particular, we consider both box shaped as well as ellipsoidal regions in this work. Our motivation for this overall approach is twofold. First, to the best of our knowledge a min-max formulation of the problem of uncertain sensor locations has not been proposed or examined to date in the context of subsurface sensing. Thus, our effort provides a new and potentially useful way of approaching this issue. Second, while min-max problems are generally quite computationally intensive, under a small perturbation assumption we obtain two very tractable algorithms (one for boxes and the second for ellipsoids) for solving the resulting inverse problem. The method exploits some convenient underlying structure of the problem and is very amenable to a parallel implementation.

1.2 Literature Survey

The problem of detecting and classifying buried objects using EMI based sensing technologies has received considerable attention in recent years in a range of application areas including UXO and landmine remediation. In the last decade or so, considerable advances have been made in the area of EMI instrumentation yielding sensors capable of providing data both in the time and frequency domains which convey far more information concerning the structure of buried objects than is the case with older metal detectors.

The problem of subsurface discrimination using EMI sensors is addressed in [2]. The authors of [2] review frequency and time domain systems, and their interrelationship and present the results of comprehensive measurements of the multiaxis EMI response of a variety of inert ordnance items, fragments and scrap metal pieces recovered from firing ranges. The extent to which the distributions of the eigenvalues of magnetic polarizability for the different classes of objects do not overlap establishes an upper bound on discrimination. For various reasons, the eigenvalues cannot always be accurately determined using data collected above a buried target. This tends to increase the overlap of the distributions, and hence worsens the discrimination performance [2].

A Bayesian decision-theoretic approach to the detection of land mines is introduced in [6]. This method incorporates the statistical properties of both the target and clutter. This method substantially reduces false alarm rates relative to the standard thresholding techniques commonly used. The development is performed for an integrated time domain pulse induction sensor, a prototype multi-channel time domain pulse induction sensor and a Geophex's GEM-3 sensor which is a broadband frequency domain device explained in details in Section 4.

In most cases where sensors are used for UXO detection and discrimination, the energy in the output of the sensor is calculated and a decision regarding the presence or absence of a target is made using this statistic. This approach leads to excessively large false alarm rates. Gao et al. in [8] introduce a decision theoretic approach for classification of metal targets using wideband EMI data. The algorithm that

is presented in this work incorporates both a theoretical model of the response of a wideband, frequency domain sensor and the uncertainties regarding the target/sensor orientation. The results presented in this work indicate that incorporating the uncertainty associated with the target/sensor relative position into the processor affords a significant performance gain over a processor that simply uses the predicted response at the mean expected target position. On the average, this method introduces a 60% improvement in discrimination performance [8] comparing to the one introduced in [6].

A portable, wide bandwidth, time-domain electromagnetic sensor system has been developed and used extensively to measure the eddy current time-decay response of a wide variety of metal targets. The sensor has demonstrated the ability to measure metal target decay times approximately 3 to 5 μs after the transmitter current is turned off and target decay time constants as short as 1.4 μs . The details for the development of this sensor is described in [13]. This sensor, called the electromagnetic target discriminator (ETD), shows potential for discriminating metal land mines from clutter.

The problem of identifying conducting objects based on their response to low frequency magnetic fields is discussed in [15]. This area of research is also referred to as magnetic singularity identification (MSI). The low frequency of the objects under study was measured for both cardinal and arbitrary orientations of the magnetic field with respect to the planes of the symmetry of the objects. Distinct negative real axis poles associated with object form the basis the real time identification given in [15]. As a solution to the $M - ary$ hypothesis testing problem, a generalized likelihood ratio test (GLRT) is presented. Best performance of the GLRT classification scheme was obtained with a single pole per object orientation.

The authors of [12] propose three phenomenological models for wideband EMI response of buried conductors such as UXO and metal parts in landmines. The models are based on analytic solutions for spheres, cylinders, and wire loops, and produce physically reasonable predictions for a variety of targets at all frequencies of interest. All three methods produce excellent fit to the data and run quickly enough to be used in data inversion methods. These three models consist of the followings

[12]:

1. A three-parameter model capable of exactly matching permeable spheres and cylinders.
2. A four-parameter model for adding capability to match signals from wire loops.
3. A five-parameter model which adds capability to match signals due to driving bands (also called rotating bands).

The authors of this work demonstrate that the five-parameter model is capable of accurately fitting the loop-like signals of driving bands.

Spatial response characteristics of an electromagnetic induction sensor as it passes over a metallic object are investigated in [7] using a simple analytical technique. In this low-frequency method, the metallic object is replaced by its equivalent electric and magnetic dipoles and then the principles of reciprocity is applied to obtain the induced EMF in a sensor coil. The analysis given in this work is for a sensor with rectangular coils. This approach (discussed in more detail in Section 2.2) is found to be adequate to understand the effects of the response characteristics of parameters such as object depth, orientation, aspect ratio and material properties [7].

A sensor response model based on empirically determined orthogonal response coefficients β is presented in [1]. This model is used for the analysis of EMI sensor data and is applied to high-quality survey data from the multi-sensor towed array detection system program (MTADS). MTADS was developed by the Naval Research Laboratory to address the problems associated by the traditional methods for buried UXO detection. The MTADS hardware includes a low magnetic signature vehicle that is used to tow linear arrays of magnetic and electromagnetic sensors to conduct surveys of large areas to detect buried UXO. Primary goals of the MTADS program include the development of a system sensitive enough to detect all buried UXO to its self-penetration depth and the integration of a precise position location and survey guidance system based on global positioning (GPS) navigating.

A new method for computing range and orientation invariant spectral signatures of buried UXO from EMI data is presented in [14]. The normalized eigenvalues of

the magnetic polarizability tensor that characterizes the target response are used as the orientation-invariant spectral signatures. The eigenvalues can be normalized with respect to depth under the assumption that a multiplicative scaling factor can be applied at all frequencies. These eigenvalues are derived by measuring the matrix elements of the polarizability tensor from above-ground spatial data and then by diagonalizing this matrix. This method is linear and does not require a nonlinear parameter search. After normalizing for depth, the eigenvalues derived from an unknown object can be compared with library eigenvalues using the L_2 norm as a goodness-of-fit measure.

Given this as background, in this work we construct a method, which is based on a physical model that is the fusion of the dipole scattering model in [7] and a parametric PAPF model elucidated in [5]. This model is analytical in the parameters of the PAPF, the (x, y, z) location of the object, and the three Euler angles(explained later in detail) [11] describing the rotation matrix. The relatively simple closed form nature of the model with respect to these parameters leads us to classification methods in which the orientation and location of the object are explicitly estimated along with the parameters needed for classification. Thus, our approach provides information regarding these geometric characteristics of the object. Also, the closed form nature of the PAPF model allows our approach to be applied with equal ease to both time and frequency domain sensor data.

1.3 Organization

The remainder of the work is organized as follows: In Chapter 2 the scattering model and the mathematical structure of the basic problem is formulated. Three very general solution methods, applicable to a wide range of sensors, are detailed in this section. Chapter 3 describes the processing method. Chapter 3.3 describes the classification method applied. Chapter 4 is devoted to a detailed examination of all proposed algorithms. Experiments using both simulated and real frequency domain sensor field data is also presented in this section. Finally conclusions and future work are provided in Chapter 5.

Chapter 2

Problem formulation and Physical Model

Spatial response characteristics of an electromagnetic sensor as it passes over a metallic object are investigated using an analytical technique. Analysis is carried out for sensors with rectangular coils. This method, which is presented with both numerical and experimental data in Section 4, is shown to be suitable to understand the effect on the response characteristics of parameters such as the spatial position, orientation, and material properties of the object.

2.1 Electromagnetic Induction Sensors

2.1.1 Bistatic Sensors

The transmitter and the receiver of a bistatic sensor are not co-located. The separation between the source and receiver is used as the major operating variable in order to interpret the data. A bistatic sensor tends to stretch or distort the signature of an isolated anomaly along the line connecting the source and receiver. For instance, a spherical object may distort into an oval shape, stretched along the source-receiver line on a contour map. Depending on the sensor orientation, the same object may look different on a contour map. This can be a problematic feature for interpreting

the data. This stretching typically becomes worse as the source-receiver separation increases [17].

2.1.2 Monostatic Sensors

Monostatic sensors are sensors with zero source-receiver separation, which eliminate stretching and provide the highest possible resolution. Hence, a monostatic sensor is the most desirable sensor for achieving high spatial resolution. There are many practical design difficulties associated with producing these sensors, and without mentioning those difficulties, we note that the GEM-3 sensor is one of the few monostatic sensors to have overcome these difficulties (for more details refer to [17]).

2.1.3 GEM-3 Sensor

The field data used in this work was obtained using the GEM-3 electromagnetic sensor. This is a fairly new sensor developed by Geophex Inc. This sensor has been used in many platforms for detecting and characterizing buried conducting targets. An especially attractive feature of this sensor is its multi-frequency capability and spatial footprint. Moreover, this sensor uses a unique transmit-bucking scheme to null the primary field at the location of the primary coil.

In a frequency-domain platform, the GEM-3 obtains a set of desired transmitter frequencies in the form of a digital bit-stream. The desired transmitter waveform for a particular survey can be obtained from this bit-stream. This sensor weighs about 5 kg and can measure up to 12 data points per second at multiple frequencies between 90 Hz to about 24 kHz [19].

GEM-3 contains a pair of concentric transmitter coils and a small receiver coil at the center. This configuration is monostatic because the coils are co-located. The design principle of the GEM-3 sensor involves two concentric transmitter coils. The details for this sensor design have been discussed by Won *et al.* in [17] and [18].

2.2 Physical Model

The analysis used in this work assumes that the object and the sensor are located in free space. We choose to ignore the very small effect of a finitely conductive host medium such as soil because of the following reasons [7]:

- In our application the effect of soil is small in comparison to the target response. This is because the conductivity contrast involved is very high (soil conductivity is typically less than 1 S/m, while target conductivity is of the order of 10^7 S/m), target depth and coil dimensions are small (less than 2 m), and frequencies used are low (typically less than 20 kHz).
- The added complexity would not change the main focus of our analysis, which is to understand the relationship of the spatial response characteristics of an object with its depth, orientation, material, shape, etc.

It is very difficult to predict the exact response profile of an electromagnetic sensor as it passes over an arbitrary metallic object. This problem becomes even more difficult when the target becomes closer to the sensor coils and when noncircular coils of finite size are used. The analytical approach to this problem is based on the work of Burrows [7], [9]. The method discussed in [9] replaces the scatterer with equivalent electric dipoles and then applies the principle of reciprocity to obtain the induced EMF in the sensor coil. Since the magnitude of the electric field is very small, one needs to assume that the object of interest scatters the incident EMI field as a dipole. Inaccuracies will occur because of the fact that the magnetic field over a typical object, in the vicinity of a coil, is non-uniform. This will violate the assumption of perfect dipoles.

The EMF, E , induced in a single-turn receive coil by a magnetic dipole \vec{M} can be shown as the following scalar product:

$$E = \frac{j\omega\mu_0}{I} \vec{H}^R \cdot \vec{M} \quad (2.1)$$

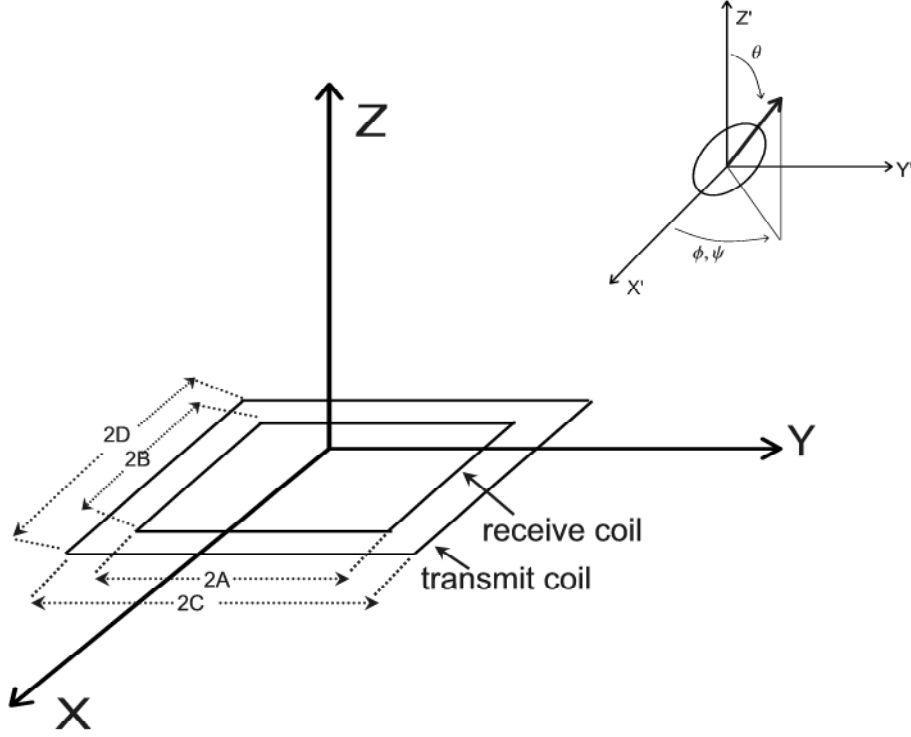


Figure 2.1: Geometry of sensor coils and target object for one sensor

where \vec{H}^R is the magnetic field intensity which would be produced at the position of the dipole by a current I flowing in the receive coil, $j = \sqrt{-1}$, ω is the radial operation frequency and μ_0 is the permeability of the free space.

Figure 2.1 depicts the coil and target geometry of a sensor. The center of the coils is located at the origin of the (x, y, z) coordinate system. The coordinates (x', y', z') , with the object center at its origin, is a translated version of (x, y, z) and is only displayed for clarity of illustration. Assuming that the target is located at (x_0, y_0, z_0) the distance $d = |z_0|$ is referred to as object depth, or simply, depth. Here, the components of the magnetic field intensity at (x_0, y_0, z_0) due to a rectangular coil with sides $2A$ and $2B$ and carrying a current I can be written as follows [7]:

$$H_x^R = \frac{I}{4\pi}(H_{x2} + H_{x4}) \quad (2.2)$$

$$H_y^R = \frac{I}{4\pi}(H_{y1} + H_{y3}) \quad (2.3)$$

$$H_z^R = \frac{I}{4\pi}(H_{z1} + H_{z2} + H_{z3} + H_{z4}) \quad (2.4)$$

where,

$$H_{x2} = -\frac{z_0}{(x_0 + A)^2 + z_0^2} \left[\frac{(y_0 - B)}{(x_0 + A)^2 + (y_0 - B)^2 + z_0^2} - \frac{(y_0 + B)}{(x_0 + A)^2 + (y_0 + B)^2 + z_0^2} \right]$$

$$H_{x4} = -\frac{z_0}{(x_0 - A)^2 + z_0^2} \left[\frac{(y_0 + B)}{(x_0 - A)^2 + (y_0 + B)^2 + z_0^2} - \frac{(y_0 - B)}{(x_0 - A)^2 + (y_0 - B)^2 + z_0^2} \right]$$

$$H_{y1} = +\frac{z_0}{(y_0 - B)^2 + z_0^2} \left[\frac{(x_0 + A)}{(x_0 - A)^2 + (y_0 - B)^2 + z_0^2} - \frac{(x_0 - A)}{(x_0 + A)^2 + (y_0 - B)^2 + z_0^2} \right]$$

$$H_{y3} = +\frac{z_0}{(y_0 + B)^2 + z_0^2} \left[\frac{(x_0 + A)}{(x_0 + A)^2 + (y_0 + B)^2 + z_0^2} - \frac{(x_0 - A)}{(x_0 - A)^2 + (y_0 + B)^2 + z_0^2} \right]$$

$$H_{z1} = -\frac{(y_0 - B)}{(y_0 - B)^2 + z_0^2} \left[\frac{(x_0 - A)}{(x_0 - A)^2 + (y_0 - B)^2 + z_0^2} - \frac{(x_0 + A)}{(x_0 + A)^2 + (y_0 - B)^2 + z_0^2} \right]$$

$$H_{z2} = +\frac{(x_0 + A)}{(x_0 + A)^2 + z_0^2} \left[\frac{(y_0 - B)}{(x_0 + A)^2 + (y_0 - B)^2 + z_0^2} - \frac{(y_0 + B)}{(x_0 + A)^2 + (y_0 + B)^2 + z_0^2} \right]$$

$$H_{z3} = -\frac{(y_0 + B)}{(y_0 + B)^2 + z_0^2} \left[\frac{(x_0 + A)}{(x_0 + A)^2 + (y_0 + B)^2 + z_0^2} - \frac{(x_0 - A)}{(x_0 - A)^2 + (y_0 + B)^2 + z_0^2} \right]$$

$$H_{z4} = +\frac{(x_0 - A)}{(x_0 - A)^2 + z_0^2} \left[\frac{(y_0 + B)}{(x_0 - A)^2 + (y_0 + B)^2 + z_0^2} - \frac{(y_0 - B)}{(x_0 - A)^2 + (y_0 - B)^2 + z_0^2} \right]$$

The magnetic moment \vec{M} depends on the electromagnetic and geometrical characteristics of the object of interest, which in turn depends on the relative orientation of the transmit coil and target [7].

The same approach can be used when dealing with sensors whose locations is only known relative to some reference point. To better understand this problem, let us assume that the positional uncertainty for our sensor is $(\delta_x, \delta_y, \delta_z)$. In that case, the center of the coils will shift from the origin to $(\delta_x, \delta_y, \delta_z)$. In order to take advantage of the physical model given above, we can simply consider the following mapping:

$$x_0 \longrightarrow x - \delta_x \tag{2.5}$$

$$y_0 \longrightarrow y - \delta_y \tag{2.6}$$

$$z_0 \longrightarrow z - \delta_z \tag{2.7}$$

which could also be considered as a shift of the coordinate axis.

The natural response of conducting and permeable targets is determined by a sum of nearly purely damped exponentials, with the damping constants strongly dependent on target's shape, conductivity, and permeability, thereby representing a potential tool for EMI discrimination of conducting and permeable targets [9].

We now consider a combination of the previously introduced physical EMI model with the model given in [9] which rigorously justifies the use of decaying exponentials in time or one-pole models in frequency for problems of this type . As seen in Figure 2.1 the transmitters and receivers are taken to be coils (not necessarily co-located)

with sides of length $2A$.

The target center is located at $r_0 = (x_0, y_0, z_0)$ in the (x, y, z) coordinate system. We are concerned with processing methods based on time or frequency domain sampled data obtained from multiple transmitter/receiver locations. Assuming, we collect M frequency samples at N combinations of transmitter/receiver locations, then under the model the j th sample at the k th location is:

$$y_{j,k} = g_k^T R^T \Lambda_j R f_k + \sigma n_{j,k} \quad (2.8)$$

where, g^T is a 3×1 vector holding the (x, y, z) components of the magnetic field produced at r_0 by a current I flowing through the receiver coil and f represents the excitation fields vector evaluated at the dipole position. Functional forms of g and f are given in Equations (2.2),(2.3) and (2.4). The variable $n_{j,k}$ is a zero mean, unit variance random variable and σ is the standard deviation of the assumed additive white Gaussian measurement noise. This formula was developed under the assumption that the positions of the sensor are known precisely relative to some fixed reference point. This condition in reality is not often met.

Λ_j is the complex-valued polarizability tensor for the k th frequency and has the following form:

$$\Lambda(\omega) = \begin{bmatrix} \lambda_1(\omega) & & \\ & \lambda_2(\omega) & \\ & & \lambda_3(\omega) \end{bmatrix} \quad (2.9)$$

where $\lambda_1, \lambda_2, \lambda_3$ are associated with one of each principle axes of the object and ω is the operating frequency. Replacing ω by t will give the time domain version of this equation. The three λ 's each are associated with one of the principal axes of the object. Here we consider a form of that model provided by [6, 5, 16]

$$\lambda_i(\omega) = \sum_{l=1}^{\infty} \frac{a_{i,l} j\omega}{p_{i,l} + j\omega} \quad i = 1, 2, 3 \quad (2.10)$$

where $p_{i,l}$ is the l th pole for the i th axis, and $a_{i,l}$ is the expansion coefficient. An inverse Fourier transform yields the time-domain version of λ :

$$\lambda_i(t) = - \sum_{l=1}^{\infty} a_{i,l} p_{i,l} e^{-p_{i,l} t} u(t) \quad (2.11)$$

with $u(t)$ the unit step function. For cylinders and disks, Carin *et al* recently provided a fast numerical method for computing the $p_{i,l}$. The model in (2.10) and (2.11) strictly holds for non-ferrous objects. In the case of ferrous objects, a DC offset in frequency or a Dirac delta function in time domain must be added to the above equations. For notational ease, in the remaining part of this chapter we will only concentrate on the non-ferrous case with the understanding that some small changes need to be made for ferrous objects.

In (2.8) R is a rotation matrix which orients the object in the space and is used to transform field quantities between a global frame of reference and the local frame of the object. The structure of R and details of Euler angles and the problems associated with them are explained in great detail in Section 2.2.1.

As explained earlier in Section 1 the magnetic polarizability tensor Λ can be diagonalized by R . Each element of the resulting matrix holds the scattering characteristics of the object along each of the three-principle axis and is referred to as PAPF.

Equation 2.8 can be re-written as:

$$y_{j,k} \equiv s_{n,k} + \sigma \omega_{j,k} \quad (2.12)$$

Gathering the data from all sensors together, the overall model can be written as:

$$y(p, a, \theta) = s(p, a, \theta) + \sigma \omega \quad (2.13)$$

where y holds the data from all sensor locations and frequency samples, s is the signal vector, n is the noise vector, p is the vector of all poles, a is the vector of all expansion

coefficients and θ holds the coordinates and Euler angles of the object.

This model assumes that the object behaves electromagnetically like a dipole. The three λ_i 's then fully summarize the scattering behavior of the object and only depend on the size, shape, and material of the object and not on the orientation and position of the object relative to the sensor. Thus, the pole and expansion coefficients make good candidates for use in a classification routine. The orientation information is explicitly contained in the matrix R while the field vectors f and g convey position information. Due to the simple, analytical nature of this model, it is quite well suited for use in a signal processing routine where operations like pole fitting and parameter estimation are accomplished using optimization routines. The complexity of these routines is substantially reduced due to our ability to use the model to compute closed form sensitivity information; essentially the derivative of the data with respect to any of the unknowns: poles, expansion coefficients, Euler angles or location coordinates. Such calculations are at the heart of any parameter-fitting scheme employing e.g. a gradient decent, conjugate gradient, or Newton type of optimization scheme.

While the utility of the model described here has been validated using real sensor data [7], generally objects do not behave exactly as dipoles. Moreover, one cannot practically use an infinite number of poles for each λ_i . Rather, a single pole per axis is the most that is typically supported by the data. In such a case, the effective pole for each axis will be dependent on the object position and orientation. The end result is that for all practical purposes model mismatch or required model reduction will force us to consider pole-based classifiers, which explicitly account for variations in the feature values. If such variations are small, then one expects success in using poles (effective poles) for classification.

2.2.1 Euler Angles

Every Euclidean change of axis can be written as the composition of three rotations (Figure 2.2). From the physical point of view this means that three parameters are required to specify a rigid rotation of axes. One of the most efficient and convenient ways of specifying these parameters is by using Euler Angles.

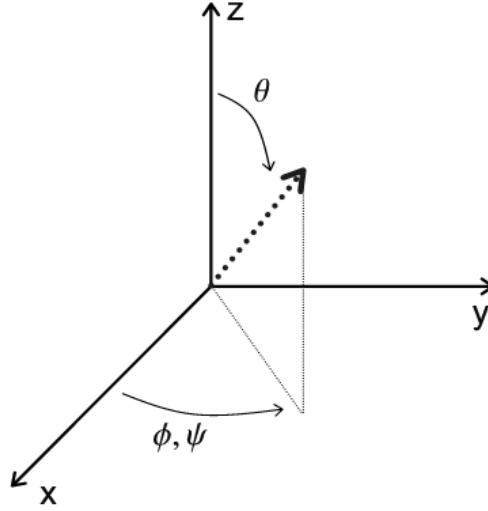


Figure 2.2: Euler Angles

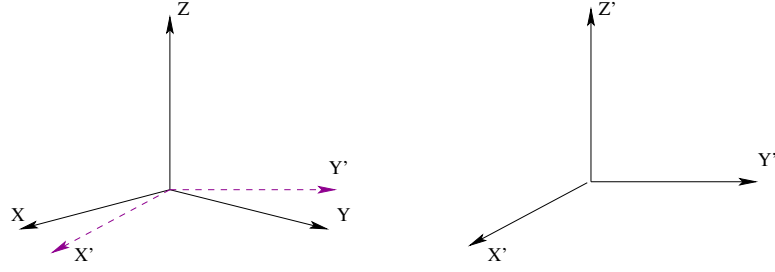
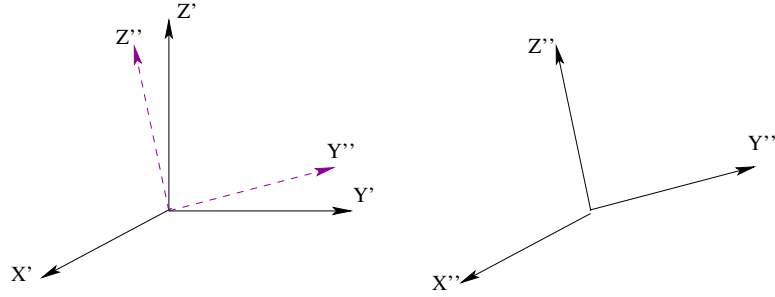
Intervals of Definition for Eulerian Angles

In order to gain a better understanding of how Euler angles can be used to specify a rigid rotation of axes, let us consider the following rotations [11]:

1. Rotation of the coordinate system about the Z axis through an angle ϕ . This corresponds to a rotation in the $X-Y$ plane of angle ϕ , leaving the Z unchanged (Figure 2.3). The matrix corresponding to such a rotation is:

$$R_1 = \begin{bmatrix} \cos \phi & -\sin \phi & 0 \\ \sin \phi & \cos \phi & 0 \\ 0 & 0 & 1 \end{bmatrix} \quad (2.14)$$

2. Rotation of the coordinate system about the X' axis through an angle θ . This corresponds to a rotation in the $Y'Z'$ plane of angle θ , leaving the X' unchanged (Figure 2.4). The matrix corresponding to such a rotation is:

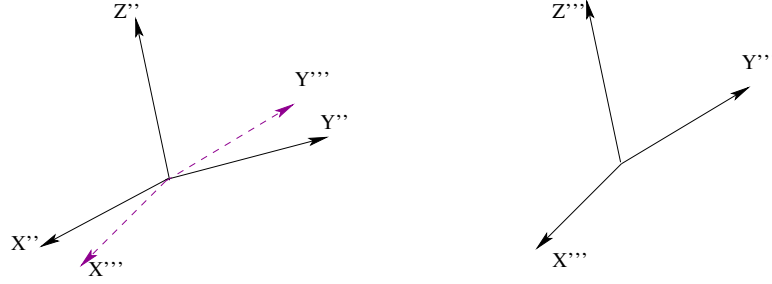
Figure 2.3: Rotation of the coordinate system about the Z axis through an angle ϕ .Figure 2.4: Rotation of the coordinate system about the X' axis through an angle θ .

$$R_2 = \begin{bmatrix} 1 & 0 & 0 \\ 0 & \cos \theta & -\sin \theta \\ 0 & \sin \theta & \cos \theta \end{bmatrix} \quad (2.15)$$

3. Rotation of the coordinate system about the Z'' axis through an angle ψ . This corresponds to a rotation in the $X''Y''$ plane of angle ψ , leaving the Z' unchanged (Figure 2.5). The matrix corresponding to such a rotation is:

$$R_3 = \begin{bmatrix} \cos \psi & -\sin \psi & 0 \\ \sin \psi & \cos \psi & 0 \\ 0 & 0 & 1 \end{bmatrix} \quad (2.16)$$

From this we can conclude that the system x_2, y_2, z_2 is obtained from x_0, y_0, z_0 by the following operation:

Figure 2.5: Rotation of the coordinate system about the Z_2 axis through an angle ψ

$$R = R_3 R_2 R_1 = \begin{bmatrix} \cos \phi \cos \psi - \sin \phi \cos \theta \sin \psi & -\cos \phi \sin \psi - \sin \phi \cos \theta \cos \psi & \sin \phi \sin \theta \\ \sin \phi \cos \psi + \cos \phi \cos \theta \cos \psi & -\sin \phi \sin \psi + \cos \phi \cos \theta \cos \psi & -\cos \phi \sin \theta \\ \sin \theta \sin \psi & \sin \theta \cos \psi & \cos \theta \end{bmatrix} \quad (2.17)$$

where matrix R is same the rotation matrix employed in Equation 2.8.

We, now, try to derive an upper and lower bounds for the Euler angles given in 2.17. Let us consider the following mapping:

$$\begin{aligned} \theta &\longrightarrow 2\pi - \theta \\ \phi &\longrightarrow \phi + \pi \mod (2\pi) \\ \psi &\longrightarrow \psi + \pi \mod (2\pi) \end{aligned} \quad (2.18)$$

and since the above mapping gives the same rotation matrix as the one shown in Figure (2.5), we can conclude that, any rotation angle θ_1 satisfying $\pi < \theta_1 \leq 2\pi$ can be realized with $\theta_0 = 2\pi - \theta_1$, where $\theta_0 \leq \pi$, $0 \leq \phi + \pi \mod (2\pi) \leq 2\pi$ and $0 \leq \psi + \pi \mod (2\pi) \leq 2\pi$. From this we can conclude that $\theta_1 > \pi$ will give the same transformation as $\theta_1 \leq \pi$. Thus the intervals of definition for the Eulerian Angles are:

$$0 \leq \phi \leq 2\pi \quad (2.19)$$

$$0 \leq \theta \leq \pi \quad (2.20)$$

$$0 \leq \psi \leq 2\pi$$

Rotational Ambiguities

One possible difficulty associated with our proposed model (2.8) is the problem of *Pole Switching*. When performing the matrix multiplication $R^T \Lambda R$, for certain Euler angles, the order of the λ 's given in (2.9) may change. As a result of the change, two completely different set of Euler Angles may give the same result once the operation $R^T \Lambda R$ is performed on them. This will clearly cause an ambiguity in the decomposition of magnetic polarization tensor. In fact, there exists five matrices O_i such that $O^T \Lambda O$ is still diagonal but with λ_i permuted. The followings demonstrates these cases:

- **Case I:** $\phi = 0, \theta = \frac{\pi}{2}, \psi = 0$

$$\begin{bmatrix} 1 & 0 & 0 \\ 0 & 0 & 1 \\ 0 & -1 & 0 \end{bmatrix} \begin{bmatrix} \lambda_1 & 0 & 0 \\ 0 & \lambda_2 & 0 \\ 0 & 0 & \lambda_3 \end{bmatrix} \begin{bmatrix} 1 & 0 & 0 \\ 0 & 0 & -1 \\ 0 & 1 & 0 \end{bmatrix} = \begin{bmatrix} \lambda_1 & 0 & 0 \\ 0 & \lambda_3 & 0 \\ 0 & 0 & \lambda_2 \end{bmatrix} \quad (2.21)$$

- **Case II:** $\phi = \frac{\pi}{2}, \theta = 0, \psi = 0$

$$\begin{bmatrix} 0 & -1 & 0 \\ 1 & 0 & 0 \\ 0 & 0 & 1 \end{bmatrix} \begin{bmatrix} \lambda_1 & 0 & 0 \\ 0 & \lambda_2 & 0 \\ 0 & 0 & \lambda_3 \end{bmatrix} \begin{bmatrix} 0 & -1 & 0 \\ 1 & 0 & 0 \\ 0 & 0 & 1 \end{bmatrix} = \begin{bmatrix} \lambda_2 & 0 & 0 \\ 0 & \lambda_1 & 0 \\ 0 & 0 & \lambda_3 \end{bmatrix} \quad (2.22)$$

- **Case III:** $\phi = \frac{\pi}{2}, \theta = \frac{\pi}{2}, \psi = \frac{\pi}{2}$

$$\begin{bmatrix} 0 & 0 & 1 \\ 0 & -1 & 0 \\ 1 & 0 & 0 \end{bmatrix} \begin{bmatrix} \lambda_1 & 0 & 0 \\ 0 & \lambda_2 & 0 \\ 0 & 0 & \lambda_3 \end{bmatrix} \begin{bmatrix} 0 & 0 & 1 \\ 0 & -1 & 0 \\ 1 & 0 & 0 \end{bmatrix} = \begin{bmatrix} \lambda_3 & 0 & 0 \\ 0 & \lambda_2 & 0 \\ 0 & 0 & \lambda_1 \end{bmatrix} \quad (2.23)$$

- **Case IV:** $\phi = 0, \theta = \frac{\pi}{2}, \psi = \frac{\pi}{2}$

$$\begin{bmatrix} 0 & -1 & 0 \\ 0 & 0 & 1 \\ 1 & 0 & 0 \end{bmatrix} \begin{bmatrix} \lambda_1 & 0 & 0 \\ 0 & \lambda_2 & 0 \\ 0 & 0 & \lambda_3 \end{bmatrix} \begin{bmatrix} 0 & 0 & 1 \\ -1 & 0 & 0 \\ 0 & 1 & 0 \end{bmatrix} = \begin{bmatrix} \lambda_3 & 0 & 0 \\ 0 & \lambda_1 & 0 \\ 0 & 0 & \lambda_2 \end{bmatrix} \quad (2.24)$$

- **Case V:** $\phi = \frac{\pi}{2}, \theta = \frac{\pi}{2}, \psi = 0$

$$\begin{bmatrix} 0 & 0 & 1 \\ 1 & 0 & 0 \\ 0 & 1 & 0 \end{bmatrix} \begin{bmatrix} \lambda_1 & 0 & 0 \\ 0 & \lambda_2 & 0 \\ 0 & 0 & \lambda_3 \end{bmatrix} \begin{bmatrix} 0 & 1 & 0 \\ 0 & 0 & 1 \\ 1 & 0 & 0 \end{bmatrix} = \begin{bmatrix} \lambda_2 & 0 & 0 \\ 0 & \lambda_3 & 0 \\ 0 & 0 & \lambda_1 \end{bmatrix} \quad (2.25)$$

Here, $R'_i = O_i R_i$ is still a valid rotation matrix. This means that extra care must be taken if we want to associate λ_1 with the x -axis, λ_2 with the y -axis and λ_3 with the z -axis of the object to avoid “swapping” of the poles.

In order to find with a solution to this problem we considered the following options:

- Sorting the λ_1 , λ_2 and λ_3 of (2.9) in an increasing order every time we perform the $R^T \Lambda R$ multiplications.
- Developing an orthogonal operator O such that $R^T \Lambda R = R^T O \Lambda O^T R$. For instance to fix the switching problem in Case I, we can set

$$O = \begin{bmatrix} 1 & 0 & 0 \\ 0 & 0 & 1 \\ 0 & 1 & 0 \end{bmatrix}$$

then,

$$\begin{aligned} \begin{bmatrix} 1 & 0 & 0 \\ 0 & 0 & 1 \\ 0 & -1 & 0 \end{bmatrix} \begin{bmatrix} 1 & 0 & 0 \\ 0 & 0 & 1 \\ 0 & 1 & 0 \end{bmatrix} \begin{bmatrix} \lambda_1 & 0 & 0 \\ 0 & \lambda_2 & 0 \\ 0 & 0 & \lambda_3 \end{bmatrix} \begin{bmatrix} 1 & 0 & 0 \\ 0 & 0 & 1 \\ 0 & 1 & 0 \end{bmatrix} \begin{bmatrix} 1 & 0 & 0 \\ 0 & 0 & -1 \\ 0 & 1 & 0 \end{bmatrix} \\ = \begin{bmatrix} \lambda_1 & 0 & 0 \\ 0 & \lambda_2 & 0 \\ 0 & 0 & \lambda_3 \end{bmatrix} \end{aligned}$$

As we have shown above, the order of the λ 's is back to its correct form. In this work, we decided to approach this issue through the use of a sorting routine. This routine re-arranges the poles in an increasing order and hence avoids any further complications that might be caused by their switching. Simplicity was the main factor for making this decision. We expect to arrive at similar results from the usage of the other method. In Section 4, we will demonstrate and compare our results in the presence and absence of this rotational ambiguity.

Chapter 3

Processing Method

Our approach to classification starts with the construction of a target signature library, which will be used in the actual processing. For each target of interest, this library will be comprised of the three effective pole and expansion coefficients, which define the PAPFs. Given that library, classification is a two-step process. First, for each target in the library, the data are used to estimate the unknown parameters associated with that model: poles, expansion coefficients, object location and object orientation. Here, we examine three estimation schemes. The first estimation scheme is used for systems in which the location of the sensor with respect to the target is known (discussed in more detail in Section 3.2.1). Our other two estimation methods are used when the position of the sensor is not exactly known to us (see Section 3.2.2 for more details). Second, using these estimates, we examine a pole-based classification scheme. Our classifier is based on using the pole estimates alone and is expected to work well in high signal to noise cases, when we can get accurate estimates of these quantities. We begin by discussing the construction of this library.

3.1 Library Construction

As discussed in Section 2.2, the pole estimates which we use for classification will have some orientation and position dependence which should be accounted for in the construction of the library and in the processing. Let us suppose that we have

data from a known target in a known position and orientation, which either has been computed using an exact computational model, or measured using an actual sensor. For the k th target in the library, we are going to use one effective pole per λ_i defined in a best fit manner as the solution to the following optimization problem

$$p_k^{eff}(\theta_0), \hat{a}(\theta_0), \hat{\theta}(\theta_0) = \arg \min_{p,a,\theta} \|y_k(\theta_0) - s(p, a, \theta)\|_2^2 \quad (3.1)$$

where θ_0 holds the true position and orientation information, y_k is the true data vector, and p and p^{eff} are vectors of three pole parameters, one per λ_i . The symbol “ $\hat{\cdot}$ ” above quantities indicate that these are fitted to data. We note that to be consistent with the estimation scheme developed in Section 3.2, here we do fit a and θ ; however we care only about the effective pole values in constructing the library. Additionally, the effective pole parameters are implicitly dependent on the specifics of the sensing system we use, including frequencies of operation and spatial sampling strategy. Hence in theory each sensing configuration will require a separate library.

While we could construct a library holding $p_k^{eff}(\theta)$ for a dense sampling of points in θ -space, here we choose a simpler approach. Specifically, for the classifier considered in Section 3.3, we look only at the first two moments of the effective pole vector averaged over θ . Mathematically, we define the mean pole vector and the associated covariance matrix respectively via

$$\bar{p}_k = \frac{1}{Q} \sum_{i=1}^Q p_k^{eff}(\theta_i) \quad (3.2)$$

$$R_k = \frac{1}{Q} \sum_{i=1}^Q (p_k^{eff}(\theta_i) - \bar{p}_k)(p_k^{eff}(\theta_i) - \bar{p}_k)^T \quad (3.3)$$

where the index i ranges over a grid of points in θ space. Thus, to summarize, the feature library we employ for classification based on pole estimates is comprised of one three-dimensional vector and one 3×3 matrix for each target of interest and each sensing system under investigation.

3.2 Parameter Estimation

3.2.1 Estimation When Sensor Locations are Known

The first stage of processing is to estimate the parameters of our model for each target in the library. We will obtain these parameter estimates for a pole-based classifier. The details of this method is further explained in Section 3.3.

We start our approach to classification by solving a problem similar to that of Equation (3.1). We could then make use of the fact that if the data did in fact come from the k th object (which is what we will ultimately be testing), then the poles should be on average \bar{p}_k . Thus under this scheme, we would not need to estimate the poles (and the expansion coefficients if we were to keep track of these as well) and we would only need to determine the elements of θ . While such an approach is feasible, it ignores the fact that we have information concerning the behavior of the pole estimates in the form of a mean vector and a covariance matrix. Hence, rather than fixing the poles in the estimation scheme we let them float but impose some bounds on their values in recognition of the fact that since we are going to be testing the fitness of the data to the k th model the poles should be constrained to be close to the average pole value for this model. Specifically we solve the constrained optimization problem:

$$\begin{aligned} \hat{p}_{1,k}, \hat{a}_{1,k}, \hat{\theta}_{1,k} &= \arg \min_{p,a,\theta} \|y - s(p, a, \theta)\|_2^2 \\ \text{subject to } [p_k]_i &\in [[\bar{p}_k]_i - 2[\sigma_k]_i, [\bar{p}_k]_i + 2[\sigma_k]_i] \end{aligned} \quad (3.4)$$

with $[\bar{p}_k]_i$ the i th element of the vector \bar{p}_k and $[\sigma_k]_i$ the square root of the i th element along the diagonal of R_k . Hence $[\sigma_k]_i$ is the estimated standard deviation of $[\bar{p}_k]_i$. The above optimization problem essentially restricts the estimates of the poles to stay within plus or minus two standard deviations of their expected value. Again, the philosophy underlying this choice is that since we will be using these estimates to test the goodness of fit of the data vector to the k th model we should encourage the parameter estimates to stay close to the model.

To solve the problem in Equation (3.4), we use the nonlinear least squares solver

available in the Optimization Toolbox of Matlab. This code makes use of a constrained Gauss-Newton algorithm for finding a local minimizer of the objective function in the neighborhood of an initial guess. We initialize the algorithm as follows: For the poles we use \bar{p}_k and we initially take the expansion coefficients to be equal to 1.0. The initial (x, y) location of the object is taken to be that point in space with the largest magnitude response in the data, while the initial depth is 1.0m from the sensor. The Euler angles are initialized all to 0.0.

The classifier used in this work (discussed in Section 3.3), is based on estimates of the poles. To allow the maximum flexibility in determining these quantities, we use the following, second estimation scheme in which the bound constraints are lifted:

$$\hat{p}_{2,k}, \hat{a}_{2,k}, \hat{\theta}_{2,k} = \arg \min_{p,a,\theta} \|y - s(p, a, \theta)\|_2^2. \quad (3.5)$$

Again, a nonlinear least squares solver is used. This time, the algorithm is initialized with $\hat{p}_{1,k}$, $\hat{a}_{1,k}$, and $\hat{\theta}_{1,k}$. We have found that by constraining the poles in the first estimation stage, we obtain high quality estimates of the position and orientation parameters. These estimates are then used to obtain strong overall estimates of all relevant parameters in the second estimation step. Thus, this appears to provide an effective means to avoid the local minimum problem associated with non-linear parameter estimation problems.

Finally, we also employ bound constraints in (3.4) for the estimates of the elements of θ . The precise values of these constraints are problem dependent and described in Chapter 4.

3.2.2 Estimation When Sensor Locations are Unknown

The goal of this section is to develop a general purpose approach to the inverse problems which explicitly accounts for the sensor location uncertainties explained in Section 1.

General Problem Formulation

For simplicity of exposition, we restrict attention to the processing of real valued data from a single, monostatic sensor. The generalizations to multiple sets of perhaps complex data from multi-static sensing systems are conceptually straightforward, but notationally burdensome. Let us then assume that the sensor stops at N nominal locations in space indexed by $1, \dots, N$. At each location, $\mathbf{r}_i = [x_i \ y_i \ z_i]^T$, a length M vector of data (e.g. samples in a time trace), \mathbf{d}_i is acquired. The sensing problem is to extract from the \mathbf{d}_i the values of a collection of parameters such as voxel values or geometric descriptors of the buried objects needed for characterization and classification. These parameters are assembled into a column vector $\boldsymbol{\theta}$ and are mathematically related to the data via a sensor model, $\mathbf{s}(\boldsymbol{\theta}; \mathbf{r}_i) \equiv \mathbf{s}_i(\boldsymbol{\theta})$, which as indicated is also dependent on \mathbf{r}_i for $i = 1, 2, \dots, N$. For what follows, we assume here that \mathbf{s} is in fact differentiable with respect to the elements of $\boldsymbol{\theta}$ and \mathbf{r}_i .

As indicated in Section 1, it is often the case that the locations of the sensor are not known precisely. To model this situation, \mathbf{r} is taken to be the sum of two components: $\mathbf{r}_{0,i}$, the nominal or expected position of the sensor, and $\delta \mathbf{r}_i$, the perturbation to $\mathbf{r}_{0,i}$. The perturbation is such that $\mathbf{r}_i = \mathbf{r}_{0,i} + \delta \mathbf{r}_i \in \mathcal{S}_i$ where \mathcal{S}_i is a region of space whose size is dictated by the predefined tolerances provided with the data. For simplicity, here we assume that these tolerances are the same for all positions. In this work, we consider algorithms based on two choices for the \mathcal{S}_i : boxes and ellipsoids. Mathematically, a box of size X in the x direction, Y in y , and Z in z centered at a point $\mathbf{r}_0 = [x_0 \ y_0 \ z_0]^T$ is defined as

$$\mathcal{B}(\mathbf{r}_0) = \left\{ \mathbf{r} = [x \ y \ z]^T \left| |x - x_0| < \frac{X}{2}, |y - y_0| < \frac{Y}{2}, |z - z_0| < \frac{Z}{2} \right. \right\}. \quad (3.6)$$

Similarly, an ellipsoid centered at \mathbf{r}_0 with axes of length X , Y and Z is:

$$\mathcal{E}(\mathbf{r}_0) = \left\{ \mathbf{r} = [x \ y \ z]^T \left| \left(\frac{x - x_0}{X} \right)^2 + \left(\frac{y - y_0}{Y} \right)^2 + \left(\frac{z - z_0}{Z} \right)^2 \leq 1 \right. \right\}. \quad (3.7)$$

Given these definitions, the problem we face is to determine the “optimal” choice of $\boldsymbol{\theta}$ given the data, \mathbf{d}_i , and knowledge of X , Y , and Z .

A Min-Max Solution Approach

A mathematical formulation of this problem requires first a definition of optimality. As is typical for problems such as these, here we take optimality to be defined in the sense of the minimum (over all $\boldsymbol{\theta}$) norm of the square error difference between the data observed and the prediction of the data provided by the model \mathbf{s} . That is an iterative algorithm is constructed which adjusts $\boldsymbol{\theta}$ to find a (local) minimum of

$$J(\boldsymbol{\theta}, \mathbf{r}_i) = \sum_i \|\mathbf{d}_i - \mathbf{s}(\boldsymbol{\theta}, \mathbf{r}_i)\|_2^2 \quad (3.8)$$

where, for a vector \mathbf{x} , $\|\mathbf{x}\|_2^2 \equiv \mathbf{x}^T \mathbf{x}$. The problem now is how to specify the \mathbf{r}_i in the \mathbf{s} in (3.8). In most all cases, the \mathbf{r}_i are set equal to their nominal values, $\mathbf{r}_{0,i}$ and a least squares estimate of $\boldsymbol{\theta}$ is found. Here though we seek to augment the minimum error notion of optimality in a manner which easily incorporates the additional knowledge we have concerning the geometry of the \mathcal{S}_i . Essentially, the problem we have here is to determine a set of primary parameters, $\boldsymbol{\theta}$, in the presence of a collection of “nuisance” parameters, the \mathbf{r}_i , which are restricted to exist in known regions of space. One common method for solving such problems is via a “min-max” formulation. This amounts to selecting that $\boldsymbol{\theta}$ which minimizes the worst error, as measured by $J(\boldsymbol{\theta}, \mathbf{r}_i)$, as \mathbf{r}_i ranges over \mathcal{S}_i . Formally, $\hat{\boldsymbol{\theta}}$, our estimate of $\boldsymbol{\theta}$, is defined as

$$\hat{\boldsymbol{\theta}} = \arg \min_{\boldsymbol{\theta}} \max_{\mathbf{r}_1 \in \mathcal{S}_1, \dots, \mathbf{r}_N \in \mathcal{S}_N} \sum_i \|\mathbf{d}_i - \mathbf{s}(\boldsymbol{\theta}, \mathbf{r}_i)\|_2^2 \quad (3.9)$$

To obtain a tractable solution to the problem, we now make the assumption that the $\delta \mathbf{r}_i$ are sufficiently small so that we can write

$$\mathbf{s}(\boldsymbol{\theta}, \mathbf{r}_i) = \mathbf{s}(\boldsymbol{\theta}, \mathbf{r}_{i,0}) + \mathbf{A}_i(\boldsymbol{\theta}) \begin{bmatrix} \delta x_i \\ \delta y_i \\ \delta z_i \end{bmatrix} \begin{bmatrix} \frac{1}{X} & & \\ & \frac{1}{Y} & \\ & & \frac{1}{Z} \end{bmatrix} = \mathbf{s}(\boldsymbol{\theta}, \mathbf{r}_{i,0}) + \mathbf{A}_i(\boldsymbol{\theta}) \delta \mathbf{r}_i \quad (3.10)$$

where \mathbf{A}_i is the matrix whose (j, k) element is the partial derivative of the j th component of the vector \mathbf{s}_i with respect to the k th element of $\delta \mathbf{r}_i$. Essentially, (3.10) is a Taylor series expansion of the model about the nominal location of the sensor. Substitution of (3.10) into (3.9) yields:

$$\hat{\boldsymbol{\theta}} = \arg \min_{\boldsymbol{\theta}} J_1(\boldsymbol{\theta}) \quad (3.11)$$

$$J_1(\boldsymbol{\theta}) = \max_{\mathbf{r}_1 \in \mathcal{S}_1, \dots, \mathbf{r}_N \in \mathcal{S}_N} \sum_i \|\mathbf{y}_i(\boldsymbol{\theta}) - \mathbf{A}_i(\boldsymbol{\theta})\delta \mathbf{r}_i\|_2^2 \quad (3.12)$$

with $\mathbf{y}_i(\boldsymbol{\theta}) \equiv \mathbf{d}_i - \mathbf{s}(\boldsymbol{\theta}, \mathbf{r}_{i,0})$. Were it not for the inner maximization, the typical approach to determine $\hat{\boldsymbol{\theta}}$ requires the use of an iterative optimization routine such as steepest decent, non-linear conjugate gradient, or a Gauss-Newton type method which exploits the underlying least squares structure of the problem. These techniques all require that the cost function, $J_1(\boldsymbol{\theta})$ is differentiable at least once in the elements of $\boldsymbol{\theta}$. For our problem, since $J_1(\boldsymbol{\theta})$ itself is the solution to an optimization problem we cannot guarantee its smoothness. Even if we could, computing gradients, Hessians and such is not particularly feasible. Thus we adopt a two level approach to determining $\hat{\boldsymbol{\theta}}$. First, a general purpose non-smooth optimization scheme (Matlab's Nelder-Mead method in fact) is used to solve the “outer” minimization problem. This leaves us with having to solve the “inner” maximization problem at each iteration of the Nelder-Mead method.

In general, (3.12) represents a numerically intensive optimization problem. Here however, there is significant structure, which greatly simplifies the situation. It is the recognition and exploitation of this structure along with the performance of the algorithm itself that we feel are the primary contributions of the work in this thesis. Two observations serve to ease the burden of the inner maximization:

1. First, because the perturbations at one sensor location are independent of those at any other location, the inner maximization in (3.11) separates and we obtain

$$\max_{\mathbf{r}_1 \in \mathcal{S}_1, \dots, \mathbf{r}_N \in \mathcal{S}_N} \sum_i \|\mathbf{y}_i(\boldsymbol{\theta}) - \mathbf{A}_i(\boldsymbol{\theta})\delta\mathbf{r}_i\|_2^2 = \sum_i \max_{\mathbf{r}_i \in \mathcal{S}_i} \|\mathbf{y}_i(\boldsymbol{\theta}) - \mathbf{A}_i(\boldsymbol{\theta})\delta\mathbf{r}_i\|_2^2 \quad (3.13)$$

Hence rather than having to solve one large maximization problem involving $3N$ variables, we can, in parallel, solve N small problems each with only 3 variables.

2. Second, both classes of \mathcal{S}_i (boxes and ellipsoids) are convex shapes. Because $\|\cdot\|_2^2$ is a convex function of its argument we are guaranteed that the maxima for each of our N problems is achieved on the boundary of \mathcal{S}_i . The implication of this fact for the box and ellipsoidal regions lead then to the two basic algorithms developed in this paper.

3.2.3 Boxes

When the regions \mathcal{S}_i are boxes, the existence of the solution to the basic maximization problem on the boundary of the box can in fact be strengthened. Specifically, it is well known that the solution must exist on one of the corners of the box. Thus, each of the maximization problems in (3.13) can be solved simply by evaluating the cost at each of the eight corners of the associated box and finding the maximum value.

3.2.4 Ellipsoids

The case of ellipsoids is a bit more involved and a bit more interesting. Since each of the maximization problems in (3.13) is structurally identical, we drop the explicit dependence on $\boldsymbol{\theta}$ from \mathbf{A} and consider the basic problem

$$\max_{\delta\mathbf{r} \in \mathcal{S}} \|\mathbf{y} - \mathbf{A}\delta\mathbf{r}\|_2^2 \quad (3.14)$$

First, we observe from (3.7) that the boundary of set \mathcal{S} can be written as:

$$\mathcal{S} = \{\delta\mathbf{r} | \delta\mathbf{r}^T \delta\mathbf{r} \leq 1\} \quad (3.15)$$

Now, since \mathcal{S} is compact (closed and bounded), if we choose any $\delta \mathbf{r}_1 \in \mathcal{S}$ and $\delta \mathbf{r}_2 \in \mathcal{S}$, then for any $\alpha \in [0, 1]$, we can say that $\alpha \delta \mathbf{r}_1 + (1 - \alpha) \delta \mathbf{r}_2 \in \mathcal{S}$. This implies that \mathcal{S} is convex. We can then take advantage of these facts and conclude that $\mathbf{A} \delta \mathbf{r}$ is also compact and convex. From this, we can conclude that \mathcal{S} is a closed and bounded convex set.

Theorem: For a closed and bounded convex set, the maximum distance of a point to the set is achieved by a point in the boundary [3].

Using the above theorem and the fact that \mathcal{S} for any optimum solution is a closed and bounded convex set, we will arrive at the following requirement:

$$\delta \mathbf{r}^T \delta \mathbf{r} = 1 \quad (3.16)$$

Using Equation 3.16, we can now re-write (3.14) as:

$$\max_{\delta \mathbf{r}^T \delta \mathbf{r} = 1} \|\mathbf{y} - \mathbf{A} \delta \mathbf{r}\|_2^2. \quad (3.17)$$

Now, let us factor \mathbf{A} using the singular value decomposition as $\mathbf{U} \mathbf{\Sigma} \mathbf{V}^T$ and re-write (3.17) as:

$$\max_{\delta \mathbf{r}^T \delta \mathbf{r} = 1} \|\mathbf{y} - \mathbf{U} \mathbf{\Sigma} \mathbf{V}^T \delta \mathbf{r}\|_2^2. \quad (3.18)$$

In our case \mathbf{A} is an $M \times 3$ matrix so that \mathbf{U} is an $M \times M$ orthonormal matrix, \mathbf{V} is a 3×3 orthonormal matrix and $\mathbf{\Sigma}$ is an $M \times 3$ matrix of all zeros except the first three elements on the main diagonal which are the non-zero singular values, σ_i $i = 1, 2, 3$, of \mathbf{A} .

Now, let us introduce $\mathbf{z} = \mathbf{V}^T \delta \mathbf{r}$ and note that $\mathbf{V}^T \mathbf{V} = \mathbf{I}$, $\mathbf{V} = \mathbf{V}^{T^{-1}}$ hence $\mathbf{V} \mathbf{V}^T = \mathbf{I}$. We can re-write Equation 3.18 as:

$$\max_{\mathbf{z}^T \mathbf{z} = 1} \|\mathbf{y} - \mathbf{U}\mathbf{\Sigma}\mathbf{z}\|_2^2 = \max_{\mathbf{z}^T \mathbf{z} = 1} \|\mathbf{U}^T \mathbf{y} - \mathbf{\Sigma}\mathbf{z}\|_2^2 \quad (3.19)$$

Let $\mathbf{W} = \mathbf{U}^T \mathbf{y}$, then

$$\max_{\mathbf{z}^T \mathbf{z} = 1} \|\mathbf{U}^T \mathbf{y} - \mathbf{\Sigma}\mathbf{z}\|_2^2 = \max_{\mathbf{z}^T \mathbf{z} = 1} \|\mathbf{W} - \mathbf{\Sigma}\mathbf{z}\|_2^2 \quad (3.20)$$

which can be re-written as:

$$\max_{\mathbf{z}_i^T \mathbf{z}_i = 1} \|\mathbf{W} - \mathbf{\Sigma}\mathbf{z}\|_2^2 = \max_{\mathbf{z}^T \mathbf{z} = 1} \left\| \begin{bmatrix} \mathbf{w}_1 \\ \cdot \\ \cdot \\ \cdot \\ \mathbf{w}_N \end{bmatrix} - \begin{bmatrix} \sigma_1 & 0 & 0 \\ 0 & \sigma_2 & 0 \\ 0 & 0 & \sigma_3 \\ 0 & \vdots & 0 \\ 0 & 0 & 0 \end{bmatrix} \begin{bmatrix} \mathbf{z}_1 \\ \cdot \\ \mathbf{z}_3 \end{bmatrix} \right\|_2^2 \quad (3.21)$$

where $i = 1, \dots, N$.

We can now, make use of the structure of $\mathbf{\Sigma}$ and the fact that an orthonormal change of variables leaves the l_2 norm of the resulting vector invariant and write (3.21) as

$$\max_{\mathbf{z}} \left\{ \sum_{i=1}^3 (w_i - \sigma_i z_i)^2 + \sum_{i=4}^N (w_i)^2 + \lambda (z_1^2 + z_2^2 + z_3^2 - 1) \right\} \quad (3.22)$$

where we have introduced λ as the Lagrange multiplier. In order to maximize the above equation, we can simply set its derivative with respect to z_i equal to zero. We will have:

$$\begin{aligned}
-2\sigma_1 w_1 + 2\sigma_1^2 z_1 &= 2\lambda z_1 \\
-2\sigma_2 w_2 + 2\sigma_2^2 z_2 &= 2\lambda z_2 \\
-2\sigma_3 w_3 + 2\sigma_3^2 z_3 &= 2\lambda z_3
\end{aligned} \tag{3.23}$$

and since $z_1^2 + z_2^2 + z_3^2 = 1$, we can solve the above equation for z_i as follows:

$$\begin{aligned}
z_1 &= \frac{2\sigma_1}{\sigma_1^2 - \lambda} w_1 \\
z_2 &= \frac{2\sigma_2}{\sigma_2^2 - \lambda} w_2 \\
z_3 &= \frac{2\sigma_3}{\sigma_3^2 - \lambda} w_3
\end{aligned} \tag{3.24}$$

Now that we have found a solution for z_i , we can solve $\delta \mathbf{r}_i = \mathbf{V}_i' \mathbf{Z}_i$ and find $\delta \mathbf{r}_i$ which is our maximization vector. Using this, we can easily find the value of the cost function given in (3.17).

3.3 Classification

In order to generate a classifier based on the estimates of the poles we use

$$\epsilon_k = (\hat{p}_k - \bar{p}_k)^T R_k^{-1} (\hat{p}_k - \bar{p}_k). \tag{3.25}$$

This Mahalanobis-type distance metric is expected to be close to zero when k is true and larger than zero when the true object is not the k th. Using ϵ_k the classification rule is defined as follows: Choose the k^* object in the library if the magnitude of ϵ_{k^*} is less than a threshold τ else say that the object under investigation is clutter. For a classifier based on the pole estimates, k^* is that index minimizing ϵ_k over all k . In

the following chapter, we examine the performance of the pole-based classification scheme.

Chapter 4

Numerical Examples

To demonstrate the theory explained in the previous chapters, we numerically test the estimation and classification methods presented using three different libraries of targets. The GEM-3 sensor was used for all of the frequency-domain experiments presented in this chapter.

4.1 Processing When Sensor Locations Are Known

4.1.1 Simulated Data

The first object library used in this work was constructed based on simulated data. The sensing system we simulated was comprised of co-located, square transmit and receive coils. These coils sampled a one half meter square area on an equally spaced 5×5 grid of measurement points. Frequency domain versions of the sensor collected complex valued data (in-phase and quadrature) at 30 logarithmically spaced frequencies between 10Hz and 30 kHz. In this part, we assume three different libraries of targets:

1. **Amorphous Targets:** The corresponding pole values of these targets is shown in Table A.1. Since no specific shape was assumed for these targets. These targets are assumed to have three unique λ_i 's.

Angle	Values Used
ϕ	$[0, \frac{\pi}{4}, \frac{\pi}{2}, 3\frac{\pi}{4}, \pi, 5\frac{\pi}{4}, 3\frac{\pi}{2}, 7\frac{\pi}{4}, 2\pi]$
θ	$[0, \frac{\pi}{8}, \frac{\pi}{4}, 3\frac{\pi}{8}, \frac{\pi}{2}, 5\frac{\pi}{8}, 3\frac{\pi}{4}, 7\frac{\pi}{8}, \pi]$
ψ	$[0, \frac{\pi}{4}, \frac{\pi}{2}, 3\frac{\pi}{4}, \pi, 5\frac{\pi}{4}, 3\frac{\pi}{2}, 7\frac{\pi}{4}, 2\pi]$

Table 4.1: Orientations Used to Construct the Simulated Data

2. **Pipe Like Targets:** The corresponding pole values of these targets is shown in Table A.2. These targets are assumed to be cylinders hence symmetric about their primary axis. They have only two unique λ_i 's.
3. **Sphere Like Targets:** The corresponding pole values of these targets is shown in Table A.3. Sphere-like targets are symmetric about their axes, thus it is safe to assume that there is only one single unique λ_i associated with these targets.

In this chapter, we will apply the model proposed in the previous sections to each of the above libraries and will compare the results obtained in the presence of the sorting routine that deals with the rotational ambiguity issues (Section 2.2.1) with the results obtained in its absence. As expected, the discrimination rate improves in a considerable fashion once the rotational ambiguity issues are out of the picture.

Library Construction

In order to construct the target library of these objects, we applied the target poles shown in Tables A.1, A.2 and A.3 to the model given in (2.10). We then set all of our expansion coefficients to be equal to one and used the model given in Equation (2.8) to obtain the scattering characteristics of each object for 729 unique orientations (given in Table 4.1).

The non-linear least squares optimization problem of (3.1) was then applied to the scattering characteristics obtained above. This time, since we were trying to construct a three-pole model (one pole per axis), we had to set i in (2.10) to be equal to three. In order to construct the feature library, our extracted effective poles were applied to (3.2-3.3). The library results for the amorphous, sphere-like and pipe-like Targets are shown in Tables 4.2, 4.3, 4.4 respectively.

Target ID	P_k with Pole Switching	P_k without Pole Switching
A1	[153.96, 474.32, 349.29]	[153.96, 474.32, 349.29]
A2	[142.20, 457.22, 239.25]	[142.20, 457.21, 239.25]
S1	[3527.40, 4546.90, 4898.60]	[4126.8, 5139.8, 6225.2]
S2	[4326.80, 5139.80, 6225.20]	[3527.4, 4546.9, 4898.6]

Table 4.2: Simulated Data Pole Library for Amorphous Targets. All poles are in units of Hz

Target ID	P_k with Pole Switching	P_k without Pole Switching
A1	[210.67, 244.02, 448.03]	[209.05, 242.22, 443.1308]
A2	[211.16, 247.31, 377.80]	[211.16, 247.31, 377.79]
S1	[5907.0, 5885.0, 3908.0]	[5851.0, 5863.2, 3842.4]
S2	[4008.6, 3981.6, 2981.4]	[3983.3, 3992.8, 2958.9]

Table 4.3: Simulated Data Pole Library for Pipe-Like Targets. All poles are in units of Hz

Target ID	P_k with Pole Switching	P_k without Pole Switching
A1	[264.90, 309.33, 358.81]	[297.53, 295.53, 302.58]
A2	[228.77, 280.03, 322.23]	[294.53, 296.47, 293.74]
S1	[3912.5, 3914.4, 4007.3]	[4116.0, 4077.9, 4113.6]
S2	[3380.7, 3409.2, 3481.9]	[3505.1, 3492.2, 3.4807]

Table 4.4: Simulated Data Pole Library for Sphere-Like Targets. All poles are in units of Hz

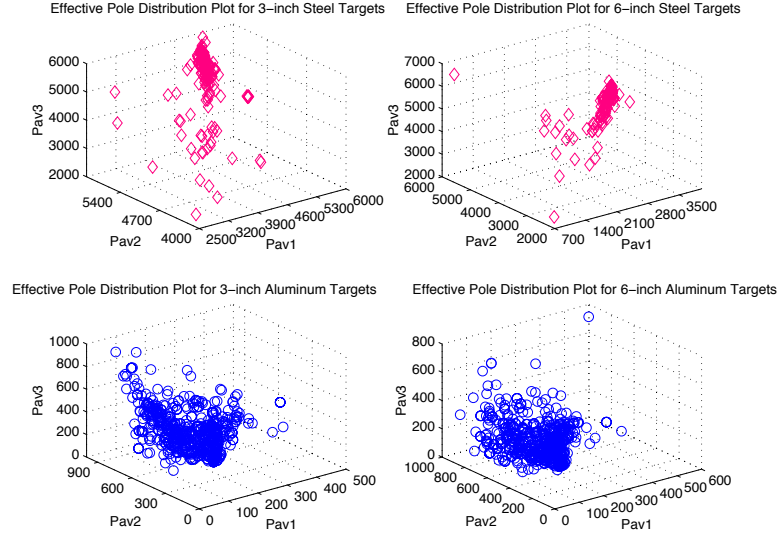


Figure 4.1: Effective Pole Distribution for Amorphous Targets With Pole Switching.

The corresponding values of \bar{p}_k for each target are shown in the above tables. The distribution of the effective poles for Aluminum and Steel amorphous, pipe-like and sphere targets in the absence and presence of pole switching is shown in Figures 4.1, 4.2, 4.3, 4.4, 4.5 and 4.6 respectively. Each point on the plot corresponds to the $(p_1^{eff}, p_2^{eff}, p_3^{eff})$ value computed from (3.1) for the i_{th} term in the summation of (2.10). As is evident, from the above tables as well as Figures, the pole characteristics of the steel objects are quite distinct from those of the aluminum; however there is very slight difference between the six and three inch versions of the same material. Hence it is anticipated that we will be able to distinguish different types of targets better than precise object. As is clear from the above tables and pictures, by using the sorting routine we arrive at pole values that are closer to ideal (two almost equal poles for pipe-like targets and three almost alike poles for sphere like targets) and pole distributions that are more clustered (tighter distributions).

Classification

The classification results of the pipe-like example are summarized into the confusion matrices of Tables 4.5 and 4.6. The element $a_{i,j}$ of this matrix demonstrates the

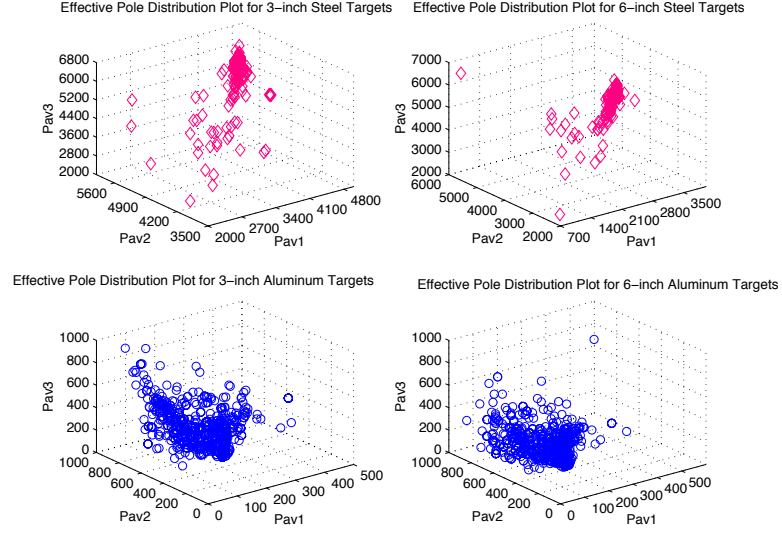


Figure 4.2: Effective Pole Distribution for Amorphous Targets Without Pole Switching.

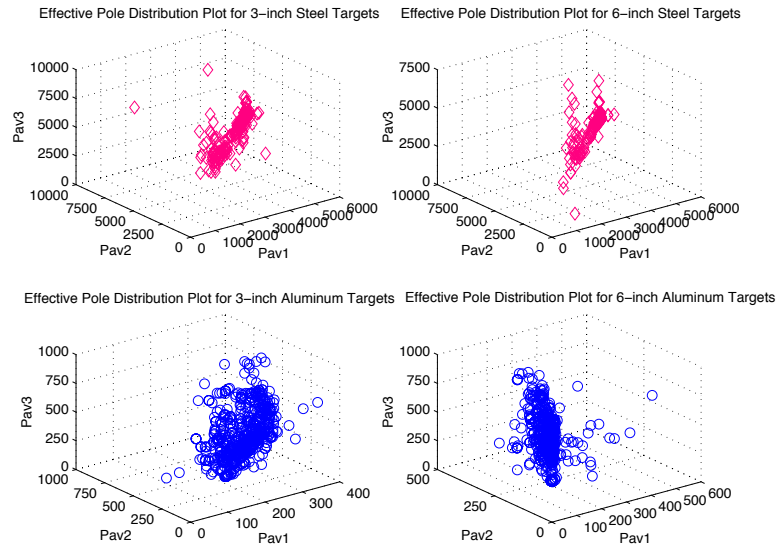


Figure 4.3: Effective Pole Distribution for Pipe-like Targets With Pole Switching.

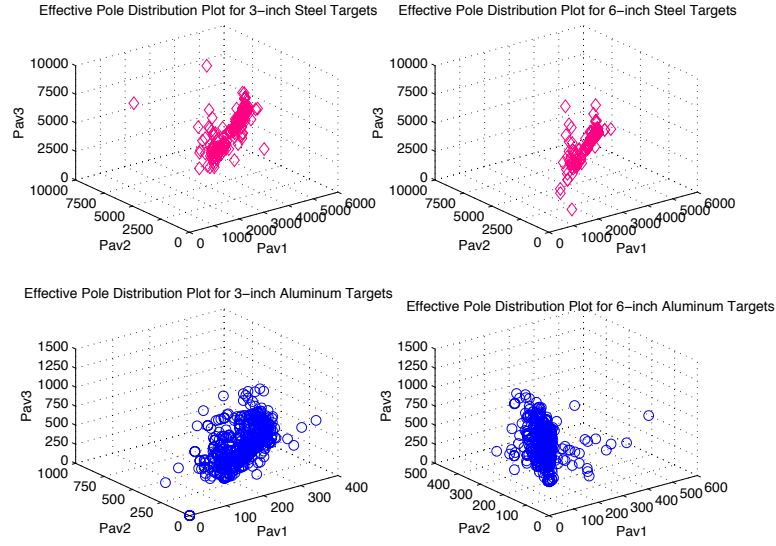


Figure 4.4: Effective Pole Distribution for Pipe-like Targets Without Pole Switching.

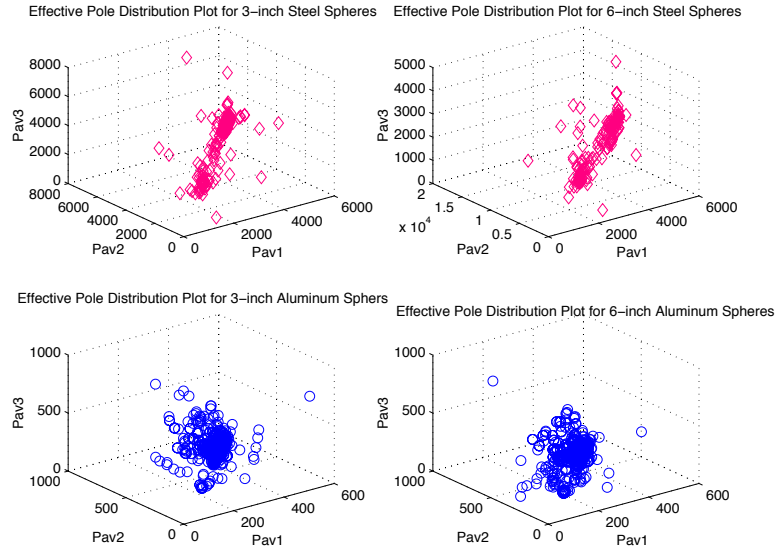


Figure 4.5: Effective Pole Distribution for Sphere-like Targets With Pole Switching.

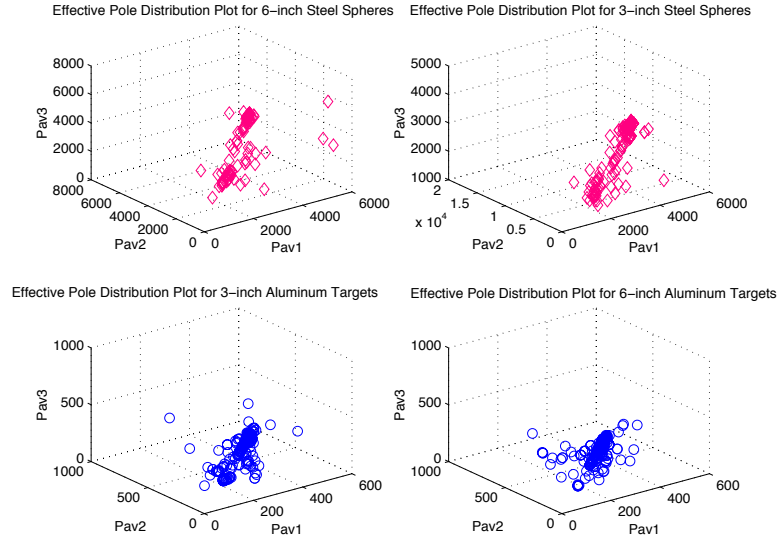


Figure 4.6: Effective Pole Distribution for Sphere-like Targets Without Pole Switching.

	A1	A2	S1	S2
A1	190	10	0	0
A2	7	193	0	0
S1	0	0	123	77
S2	0	0	73	127

Table 4.5: Classification Results for Monte Carlo Analysis without Pole Switching

number of times that object i was the true target and object j was detected. Direct comparison of these matrices verifies our claim that dealing with orientation ambiguity will improve the discrimination rate.

The quantities given in this table were estimated via Monte Carlo analysis. Specifically 200 separate runs were generated where we randomized over object type (four classes per library), object location, orientation and noise. The bounds on the various quantities are provided in Table 4.7. For each Monte Carlo run, the value of the associated parameter was selected at random with the upper and lower limits respectively set to the minimum and maximum bounds for that quantity.

In order to give the reader a sense of how the simulation results for each one of

	A1	A2	S1	S2
A1	184	16	0	0
A2	9	191	0	0
S1	0	0	79	121
S2	0	0	136	64

Table 4.6: Classification Results for Monte Carlo Analysis with Pole Switching

Min x coordinate	0.25 m
Max x coordinate	0.75 m
Min y coordinate	0.25 m
Max y coordinate	0.75 m
Min Depth	-0.25 m
Max Depth	-0.75 m
Min Euler Angle	0 rad
Max Euler Angle	2π rad

Table 4.7: Bounds for Monte Carlo Analysis

the above targets look like, here (Table 4.8) we present some of the results from the Monte Carlo simulations. The quantities shown under “Highest Score” demonstrate the corresponding ϵ_k (previously introduced in Section 3.3). “Next Highest” represent the next highest score.

4.1.2 The Geophex Pipe Data

The data for our second sensing system comes from the GEM-3 data. The GEM-3 sensor by Geophex has been used successfully in many environmental sites and can detect small targets, such as UXO and landmines, providing the highest spatial resolution of any extant technology. The current GEM-3 operates in a bandwidth from 30 HZ to 24 KHz. The Geophex test site in Rayleigh, NC, specially designed by Geophex Inc., is a 10×10 test site. This test site, shown in Figure 4.8, contains a total of 21 metal pipes of various lengths and diameters. The descriptions and details of these targets are shown in Table 4.9.

The ground truth data for this target library was obtained by the authors of [10] in known positions and orientations using an actual GEM-3 sensor. In order to construct the library, we used the aforementioned data to extract one pole per axis defined in a best fit manner as the solution to the optimization problem of (3.1). We then constructed our library of targets based on the first two moments of the extracted effective pole vectors averaged over θ (3.2-eq21). The mean pole parameters of these objects are plotted in pole-space in Figure 4.7 and shown in Table 4.9. Each point on the plot reflects the $(\bar{p}_1, \bar{p}_2, \bar{p}_3)$ value computed from the corresponding target in the library. The target library for these targets is shown in Table 4.1.2.

The scattering characteristics of the targets shown in Figure 4.8 was also acquired by the authors of [10] at a line spacing of 25 cm using the dead reckoning method. The operator handheld the GEM-3 and walked steady toward an end of the line marker while maintaining the sensor height at about 20 cm above the ground. The GEM-3 collects about 8-10 data points per second, which results in a data interval of about 15 cm for a typical walk speed. The data obtained over each line is then equally distributed along the line; assuming that the line was straight and the walking

True Target	Estimated Target	Pole Switching	Smallest Distance	Next	Correct
A1 pipe-like	A1 pipe-like	No	2.1684	641.63	Yes
A1 pipe-like	A1 pipe-like	No	13.520	716.98	Yes
A2 pipe-like	A2 pipe-like	No	2.6561	974.80	Yes
A2 pipe-like	A2 pipe-like	No	12.639	1224.1	Yes
A1 pipe-like	A1 pipe-like	Yes	3.4853	5667.7	Yes
A1 pipe-like	A1 pipe-like	Yes	44.266	4169.1	Yes
A2 pipe-like	A2 pipe-like	Yes	6.7232	820.27	Yes
A2 pipe-like	A2 pipe-like	Yes	30.658	877.48	Yes
S1 pipe-like	S1 pipe-like	No	1.0000	370.00	Yes
S1 pipe-like	S2 pipe-like	No	660.00	37434	No
S2 pipe-like	S1 pipe-like	No	150.00	438.00	No
S2 pipe-like	S2 pipe-like	No	1.0000	30.000	Yes
S1 pipe-like	S1 pipe-like	Yes	1.0000	7267.0	Yes
S1 pipe-like	S2 pipe-like	Yes	937.00	19307	No
S2 pipe-like	S1 pipe-like	Yes	113.00	4798.0	No
S2 pipe-like	S1 pipe-like	Yes	122.00	3214.0	No
A1 sphere-like	A1 sphere-like	No	0.6887	553.93	Yes
A1 sphere-like	A1 sphere-like	No	1.3566	504.53	Yes
A2 sphere-like	A2 sphere-like	No	1.1108	4340.3	Yes
A2 sphere-like	A2 sphere-like	No	1.7312	1211.3	Yes
A1 sphere-like	A1 sphere-like	Yes	6.4014	800.94	Yes
A1 sphere-like	A1 sphere-like	Yes	37.431	577.50	Yes
A2 sphere-like	A2 sphere-like	Yes	1.6481	523.08	Yes
A2 sphere-like	A2 sphere-like	Yes	31.142	598.78	Yes
S1 sphere-like	S1 sphere-like	No	1.6000	7061.0	Yes
S1 sphere-like	S2 sphere-like	No	107.00	808.00	No
S2 sphere-like	S1 sphere-like	No	1.0000	238.00	No
S2 sphere-like	S2 sphere-like	No	32.500	2113.0	Yes
S1 sphere-like	S2 sphere-like	Yes	430.00	2020.0	No
S1 sphere-like	S2 sphere-like	Yes	10.000	59540	No
S2 sphere-like	S2 sphere-like	Yes	47.000	158.00	Yes
S2 sphere-like	S2 sphere-like	Yes	43.000	2020.0	Yes

Table 4.8: Classification Results for Monte Carlo Analysis

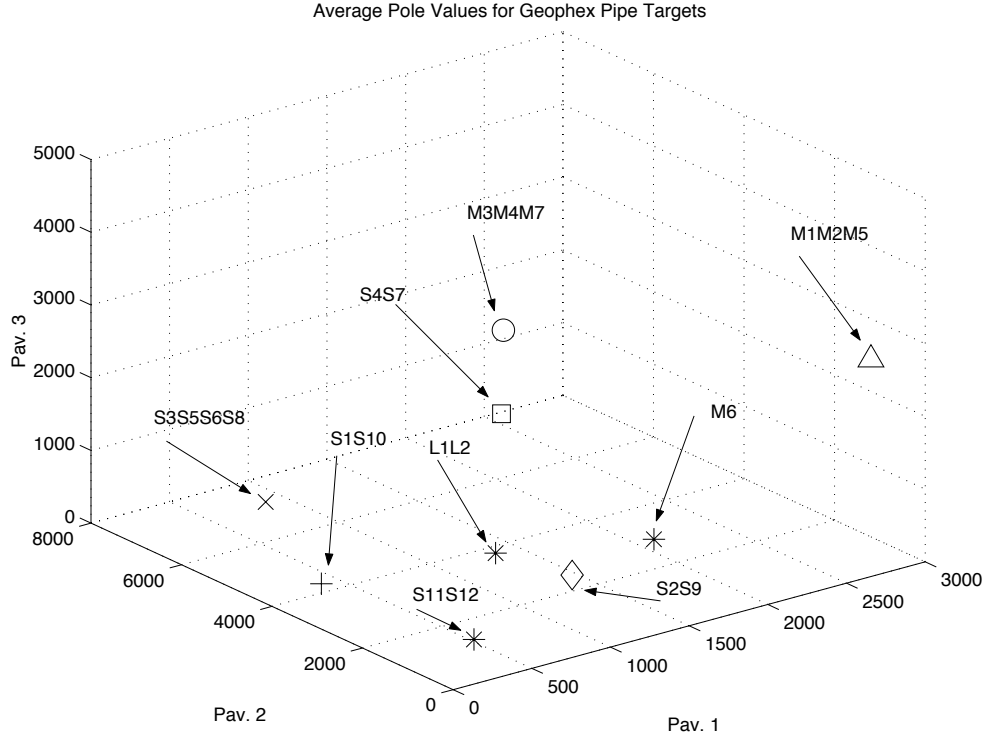


Figure 4.7: Pole Locations for Geophex Data Library

Target ID and Description	Average Poles (KHz)
L1,L2 : 15.5cm * 50.8cm Steel Pipe	[0.2411 , 3.7479 , 0.2411]
M1,M2,M5 : 7.90cm * 15.7cm Steel Pipe	[0.8310 , 1.9514 , 0.8310]
M3,M4,M7 : 6.40cm * 30.5cm Steel Pipe	[2.7837 , 0.4442 , 2.7837]
S1,S10 : 2.00cm * 10.2cm Steel Pipe	[0.5406 , 6.0202 , 0.5406]
S3,S5,S6,S8 : 4.10cm * 15.2cm Steel Pipe	[0.4317 , 0.4317 , 3.4187]
S4,S7 : 4.10cm * 10.2cm Steel Pipe	[0.4481 , 0.4481 , 4.5517]
M6 : 6.4cm * 30.5cm Aluminum Pipe	[1.2929 , 0.0590 , 1.2929]
S2,S9 : 2.30cm * 15.2cm Aluminum Pipe	[0.9016 , 0.5065 , 0.9016]
S11,S12 : 2.30cm * 15.2cm Copper Pipe	[0.3189 , 0.6472 , 0.3189]

Table 4.9: GEM 3 Pipe Data Pole Library: All dimensions in the "Description Column" are in cm. All poles are in units of kHz.

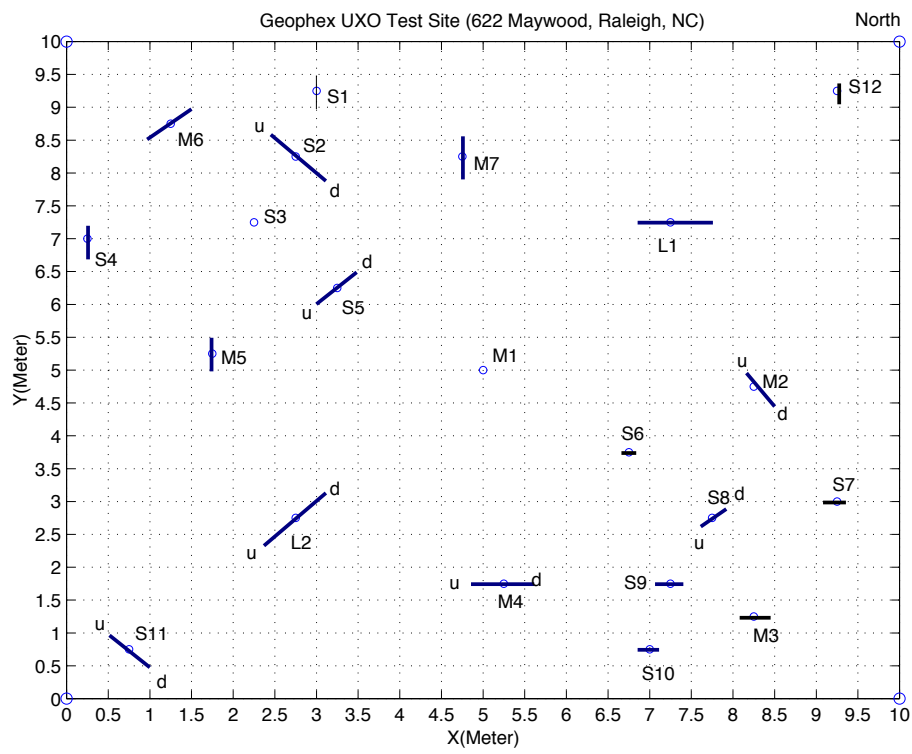


Figure 4.8: Geophex UXO Site, Rayleigh, NC

True Target	Orientation	Estimated	Result	Smallest Distance	Next
L1	Horizontal	L2	Correct	0.0001	0.2954
L2	45 Degrees	L2	Correct	0.2094	0.2970
M1	Vertical	M1	Correct	0.0083	0.0861
M2	45 Degrees	M1	Correct	0.0870	0.1513
M5	Horizontal	M1	Correct	0.0076	0.0172
M3	Horizontal	M3	Correct	0.0002	0.0008
M4	45 Degrees	M4	Correct	0.0991	0.3370
M7	Horizontal	M1	Misclassification	0.0827	0.1086
M6	Horizontal	M6	Correct	0.0082	0.0873
S1	Horizontal	M3	Misclassification	0.0027	0.0071
S10	Horizontal	S1	Correct	0.1246	0.2152
S9	Horizontal	M6	Misclassification	0.0001	0.0010
S2	45 Degrees	S2	Correct	0.0188	0.0232
S3	Vertical	M1	Misclassification	0.0339	0.0494
S5	Horizontal	M1	Misclassification	0.0083	0.0813
S6	Horizontal	M1	Misclassification	0.0819	0.8554
S8	Horizontal	S8	Correct	0.0083	0.0183
S7	Horizontal	S7	Corrcet	0.0603	0.0782
S4	Horizontal	S4	Correct	0.0654	0.0824
S11	45 Degrees	S11	Correct	0.0011	0.0044
S12	Horizontal	S11	Correct	0.0004	1.2615

Table 4.10: GEM 3 Pipe Data Results

speed was constant. The position error for such data could be as big as 20 cm due to uneven walking speed and incorrect walking path. The errors associated with the sensor height could be more than 5 cm [10]. Table 4.10 demonstrate the results of the classification algorithm for this data set.

4.1.3 The JPG-IV Data

The Naval Explosive Ordnance Disposal Technology Division, under contract to the Army Environmental Center (AEC), has released raw data collected at Jefferson

Target ID	Type	Description
3	Ordnance	81 mm Mortar
33	Ordnance	20 mm HE
51	Ordnance	51 mm HE
104	Ordnance	90 mm AP
118	Ordnance	57 mm Without Fuze
124	Ordnance	81 mm Mortar
141	Ordnance	90 mm AP
148	Ordnance	105 mm

Table 4.11: JPG-IV GEM 3 Targets

Target ID	Average Poles (KHz)
20 MM	[3.6280, 6.8990, 3.6280]
57 MM	[21.725, 4.6114, 4.6114]
60 MM	[9.5678, 4.4538, 5.0825]
81 MM	[7.0851, 7.0851, 2.9756]
90 MM	[2.9232, 2.9232, 3.6104]
105 MM	[6.1350, 6.1350, 1.1696]

Table 4.12: JPG-IV GEM 3 Data Pole Library: All dimensions in the "Description Column" are in cm. All poles are in units of kHz.

Proving Ground (JPG) by the Advanced Technology Demonstration (ATD) Program. This is the fourth in a series of ATD's designed to test current capabilities of detection, characterization, discrimination, and remediation of buried unexploded ordnance (UXO). Phase IV was strictly a discrimination exercise where locations of possible inert buried ordnance targets were given to the demonstrators in advance.

In order to construct the library, we used the aforementioned data to extract one pole per axis defined in a best fit manner as the solution to the optimization problem of (3.1). We then constructed our library of targets based on the first two moments of the extracted effective pole vectors averaged over θ (3.2-eq21). The library we considered here consists of seven targets. The descriptions and details of these targets are shown in Table 4.11.

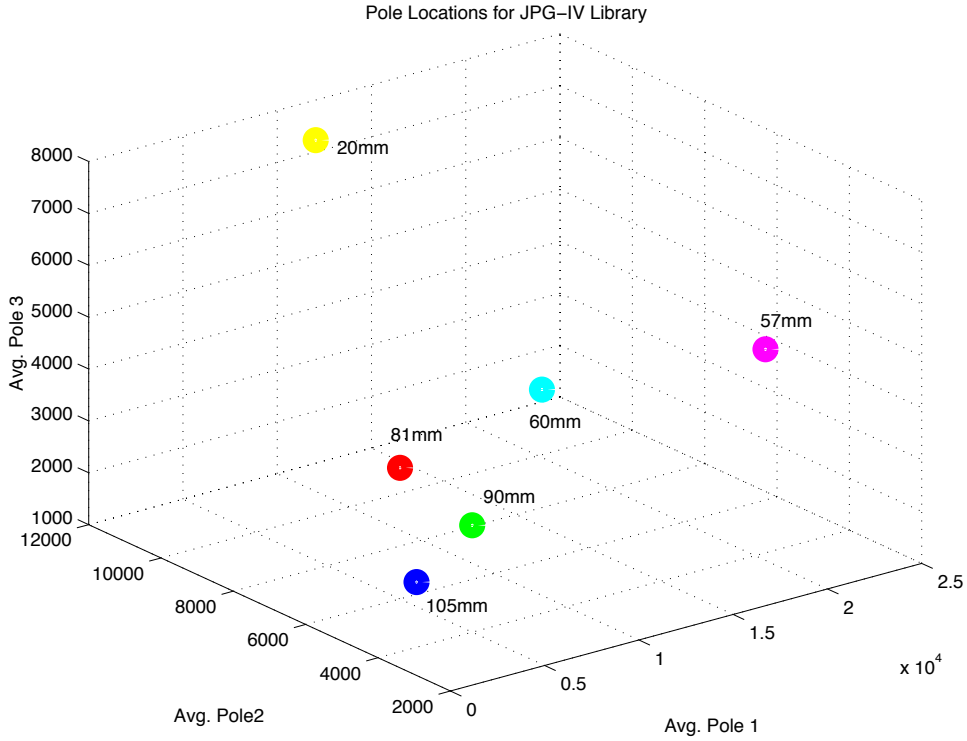


Figure 4.9: Pole Locations for JPG-IV Data Library

The mean pole parameters of our objects are plotted in pole-space in Figure 4.9 and shown in Table 4.12. Each point on the plot reflects the $(\bar{p}_1, \bar{p}_2, \bar{p}_3)$ value computed from the corresponding target in the library.

The scattering characteristics of the targets shown in figure was also acquired by the authors of [10] at a line spacing of 25 cm. Table 4.13 demonstrate the results of the classification algorithm for this data set.

Number	True Target	Estimated	Result	Highest Score	Next Highest
51	60MM	60MM	Correct	0.6572	0.7736
3	81MM	81MM	Correct	0.0034	0.0321
33	20MM	20MM	Correct	0.0182	0.2898
141	90MM	90MM	Correct	0.0057	0.0058
148	105MM	105MM	Correct	0.0167	0.0506
118	57MM	90MM	Misclassification	0.0001	0.0004
124	81MM	81MM	Correct	0.0078	0.0148
104	90MM	90MM	Correct	0.0038	0.3720

Table 4.13: JPG-IV Data Results

4.2 Processing When Sensor Locations Are Unknown

4.2.1 Ellipsoids

The pole, orientation, location and thus all the library information used here are the same as the information used in Section 4.1.1. The only difference is that, here, we assume that the location of the sensors are unknown. Thus in addition to randomizing over orientation and spatial position of the targets, we also select the location of the sensors at random. Here, we assume that the location of the sensor can deviate by as much as 5cm in each direction.

The classification results of this part example are summarized into the confusion matrix of Table 4.14. The element $a_{i,j}$ of this matrix demonstrates the number of times that object i was the true target and object j was detected. The quantities given in this table were estimated via Monte Carlo analysis. The results obtained here are from 200 separate runs were generated where we randomized over object type (four classes per library), object location, orientation, noise, and sensor locations. For each Monte Carlo run, the value of the associated parameter was selected at random with the upper and lower limits respectively set to the minimum and maximum bounds for that quantity (Table 4.7).

	A1	A2	S1	S2
A1	198	2	0	0
A2	4	196	0	0
S1	0	0	166	34
S2	0	0	41	159

Table 4.14: Classification Results for Unknown Sensor Locations (Ellipsoids)

	A1	A2	S1	S2
A1	191	9	0	0
A2	7	193	0	0
S1	0	0	146	54
S2	0	0	75	125

Table 4.15: Classification Results for Unknown Sensor Locations (Boxes)

4.2.2 Boxes

This experiment is very similar to the one performed in Section 4.2.1. Here instead of optimizing around an ellipsoid, we optimize around a $1 \times 1 \times 1$ cube. The optimization results of 200 separate runs for this section are also summarized into a confusion matrix (see Table 4.15).

Clearly, results obtained in this section are directly related to the size of the shape in which the optimization is carried out. Here, the ellipse used to in part 4.2.1 is large enough to fit the cube of 4.2.2 inside. This justifies the improvement in the results when ellipses are used.

Chapter 5

Conclusion and Future Work

In this work, we studied a number of statistically motivated, model-based options for object classification using spatially sampled time and frequency domain EMI data. The exact position and orientation of the targets under study are unknown. Basic classification algorithms were developed and tested. We also developed a theoretical model for handling sensor positional uncertainties.

The results obtained in Section 4 look very promising. In the case of our test data, we showed that our algorithms are capable of reaching very good discrimination results. Our algorithms even managed to perform very well in the presence of real field data.

Preliminary results using simulated and real field data are promising and indicate there is much work to be done in the future.

The followings summarize the possible future work that can be carried out in this area:

1. Euler angles and their effect on discrimination can be considered as a very interesting potential area of research.
2. Further study of time-domain sensors. In this work we only focused on frequency domain sensors. Analytical performance evaluation of the proposed methods for sensors that operate in time domain is a rich and diverse field with many potential areas for further studies.

3. Study of alternate classifiers such as data or data residual based classifiers. The pole-based classification statistic assumes that the effective pole parameters as a function of object location and orientation cluster into an ellipsoid. The plots presented in this work show that while the effective poles for different objects do form unique clusters, they are far from ellipsoidal. Thus it may be useful to consider alternate classification schemes such as a linear discriminate function.
4. More rigorous error analysis when processing data obtained from sensors whose locations are unknown. It would be useful to take a more careful, quantitative look at the role of parameter estimation errors, pole switching as well as sensor noise in the ultimate performance of the different classification scheme.

Appendix A

Pole Values for Monte Carlo Analysis

Target Id	Description	Pole Values (Hz)					
A1	First Aluminum Target		111.4126	450.0293	118.8830		
			121.9301	450.0293	153.3112		
			147.0808	450.0293	225.0771		
			185.3036	450.0293	337.1187		
A2	Second Aluminum Target		111.0252	264.8840	115.7203		
			111.4126	265.4070	125.4320		
			114.6415	269.7660	144.7025		
			121.9301	279.6056	173.9528		
S1	First Steel Target	$1e4 \times$	0.3390	1.1680	0.3600		
			0.3710	1.1680	0.4700		
			0.4480	1.1680	0.6900		
			0.5640	1.1680	1.0300		
S2	Second Steel Target	$1e3 \times$	3.3938	9.6687	3.8209		
			3.4922	9.6687	4.4079		
			3.7142	9.6687	5.2989		
			4.0455	9.6687	6.5016		

Table A.1: Pole Values for Monte Carlo Analysis for Amorphous Targets

Target Id	Description	Pole Values(Hz)					
A1	Three-inch Aluminum Pipe		118.8	118.8	111.4		
			153.3	153.3	121.9		
			225.1	225.1	147.1		
			337.1	337.1	185.3		
A2	Six-inch Aluminum Pipe		125.4	125.4	111.4		
			144.7	144.7	114.6		
			174.0	174.0	121.9		
			213.4	213.4	132.8		
S1	There-inch Steel Pipe		3600	3600	3390		
			4700	4700	3710		
			6900	6900	4480		
			10300	10300	5640		
S2	Six-inch Steel Pipe		3394	3821	3821		
			3492	4408	4408		
			3714	5299	5299		
			4046	6502	6502		

Table A.2: Pole Values for Monte Carlo Analysis for Pipe Like Targets

Target Id	Description	Pole Values (Hz)			
A1	Three-inch Radius Aluminum Sphere		111.4126	111.4126	118.8830
			121.9301	121.9301	153.3112
			147.0808	147.0808	225.0771
			185.3036	185.3036	337.1187
A2	Six-inch Radius Aluminum Sphere		111.4126	111.4126	125.4320
			114.6415	114.6415	144.7025
			121.9301	121.9301	173.9528
			132.8060	132.8060	213.4376
S1	Three-inch Radius Steel Sphere	$1e4 \times$	0.3390	0.3390	0.3600
			0.3710	0.3710	0.4700
			0.4480	0.4480	0.6900
			0.5640	0.5640	1.0300
S2	Six-inch Radius Steel Sphere	$1e3 \times$	3.3938	3.3938	3.8209
			3.4922	3.4922	4.4079
			3.7142	3.7142	5.2989
			4.0455	4.0455	6.5016

Table A.3: Pole Values for Monte Carlo Analysis for Sphere Like Targets

Bibliography

- [1] Bruce J. Barrow and H. H. Nelson, “Model-Based Characterization of Electromagnetic Induction Signatures Obtained with the MTADS Electromagnetic Array”, IEEE Transactions on Geoscience and Remote Sensing, Volume 39, No. 6, June 2001, p.1279-1285.
- [2] Thomas H. Bell, Bruce J. Barrow and Jonathan T. Miller, “Subsurface Discrimination Using Electromagnetic Induction Sensors”, IEEE Transactions on Geoscience and Remote Sensing, Volume 39, No. 6, June 2001, p.1286-1293.
- [3] Boyd, S., Vandenberghe, L. “Convex Optimization”, Winter Quarter 2001, Stanford University.
- [4] M.L. Burrows, “A theory of eddy current flaw detection”, 1964.
- [5] Lawrence Carin, Haitao Yu, Yacine Dalichaouch and Carl Baum, “On the Wideband EMI Response of a Rotationally Symmetric Permeable and Conducting Target”, IEEE Transactions on Geoscience and Remote Sensing, Vol 39, No. 6, June 2001.
- [6] L.Collins, P.Gao and L. Carin, “An Improved Bayesian Decision Theoretic Approach for Landmine Detection”, IEEE Transactions on Geoscience and Remote Sensing, Volume 38, May 2000, p.1352-1361.
- [7] Yogadhis Das, John E. McFee, Jack Toews and Geogory C. Stuart, “Analysis of an Electromagnetic Induction Detector For Real-Time Location of Buried Objects”, IEEE Transactions on Geoscience and Remote Sensing, Volume 28, No. 3, May 1990, p.278-288.

- [8] P. Gao, L. Collins, P. M. Garber, N. Geng and L. Carin, "Classification of Landmine-LIKE Metal Targets Using Wideband Electromagnetic Induction", IEEE Transactions on Geoscience and Remote Sensing, Volume 38, No. 3, May 2000, p.1352-1361.
- [9] Norbert Geng, Carl E. Baum and Lawrence Carin, "On the Low-Frequency Natural Response of Conducting and Permeable Targets", IEEE Transactions on Geoscience and Remote Sensing, Volume 39, No. 1, January 2001, p.374-359.
- [10] Haoping Huang and I.J. Won, "Characterization of UXO-like Targets USING Broadband Electromagnetic Induction Sensors", Geophex, Ltd.
- [11] Sadri Hassani, "Foundations of Mathematical Physics", MA, Allyn and Bacon, 1991
- [12] Jonathan T. Miller, Thomas H. Bell, Judy Soukup and Dean Keiswetter, "Simple Phenomenological Models for Wideband Frequency-Domain Electromagnetic Induction", IEEE Transactions on Geoscience and Remote Sensing,
- [13] Carl V. Nelson, Charles B. Copperman, Wolfger Schneider, Douglas S. Wenstrand and Dexter G. Smith, "Wide Bandwidth Time-Domain Electromagnetic Sensor for Metal Target Classification", IEEE Transactions on Geoscience and Remote Sensing, Volume 39, No. 6, June 2001.
- [14] Stephen J. Norton and I.J. Won, "Identification of Buried Unexploded Ordnance from Broadband Electromagnetic Induction Data", IEEE Transactions on Geoscience and Remote Sensing, Volume 39, No. 10, October 2001, p.2253-2261.
- [15] L. S. Riggs and J. E. Mooney and D. E. Lawrence, "Identification of Metallic Mine-Like Objects Using Low Frequency Magnetic Fields", IEEE Transactions on Geoscience and Remote Sensing, Volume 39, No. 1, January 2001, p.56-66.
- [16] Gary Sower, John Endsley and Ed Christy, "Discrimination of Metal Land Mines from Metal Clutter: Results of Field Tests", SPIE Conference on Detection of Mines and Minelike Targets, April 1999, p.78-88.

- [17] I.J. Won, D. A. Keiswetter, D. R. Hanson , E. Novikova, and T. M. Hall, “A Monostatic Broadband Electromagnetic Induction Sensor”, JEEG, Volume 2, Issue 1, March 1993, p.53-64.
- [18] I. J. Won, “Apparatus and Method for Detecting a Weak Inducted Magnetic Field by Means of Two Concentric Transmitter Loops” ,United States Patent, Patent Numeber 5,557,206, Sept 17, 1996.
- [19] I.J. Won, Dean Keiswetter and Elena Novikova, “Electromegnetic Induction Spectroscopy”,JEEG, Volume 3, Issue 1, March 1998, p.27-40.